國立臺灣大學電機資訊學院電信工程學研究所

碩士論文

Graduate Institute of Communication Engineering
College of Electrical Engineering & Computer Science
National Taiwan University

Master Thesis

近場通訊系統之天線耦合分析

Analysis of Antenna Coupling in Near-Field Communication Systems

陳晏笙
Yen-Sheng Chen

指導教授：李學智 博士

Advisor: Hsueh-Jyh Li, Ph.D.

中華民國 98 年 6 月

June, 2009

國立臺灣大學碩士學位論文
口試委員會審定書

近場通訊系統之天線耦合分析

Analysis of Antenna Coupling in Near-Field Communication Systems

本論文係陳晏笙君（R96942002）在國立臺灣大學電信工程學研究所完成之碩士學位論文，於民國 98 年 06 月 13 日承下列考試委員審查通過及口試及格，特此證明

口試委員：

李景熙（指導教授）

陳俊雄　江衍偉

廖宏宗　楊成發

系主任、所長　王暉

致謝

很榮幸能在台大電信所碩士班就讀兩年。首先要感謝指導教授李學智教授。老師身教謙虛而正義的品格，鼓勵我們要將台大的栽培回饋社會；提供我們最多的研究資源，使實驗室有自由而積極的學風。感謝陳士元教授，這一年來多次和老師隔海語音討論，從中學習到研究的方法、思考邏輯，以及做學問的態度；老師總是不厭其煩的指導我許多細節，並且幫助我修改投稿的期刊論文。因為兩位老師的指導，使我在研究所的成長遠超出大學畢業時的自我期許，也讓我有信心迎接下個階段博士班的挑戰。其次，我也要感謝口試委員陳俊雄教授、江衍偉教授、楊成發教授、唐震寰教授給我的建議，使我的論文更完備。

我很喜歡這一年來實驗室的研究風氣，認識了許多好朋友。感謝博士班學姊文方，學長柏仁、均哲、偉傑、家杰、念恩、易洵、貴程、蒲平日之照顧。謝謝宗穎，除了在研究上幫助我，平時我們一起聊天、打球、玩樂，都會是我珍貴的回憶。感謝建伯幫我修改論文的英文，以及平日的討論與協助。也謝謝同學得勝，曾經陪我在無反射室量測到半夜才回家。謝謝學弟李明，和你聊運動比賽總是很有趣；而且玩 MVP 當我被拉開，你都會投幾個內角高讓我打。學弟昱超，你是我看過最乖的小孩，做事總是能讓人放心。還有貼心的力涵，畢業典禮從你們手中接過拼圖卡片的那一刻，我真的很感動。因為有你們這些好朋友，讓我來實驗室都覺得很開心。感謝好友奕嘉，雖然我們高中是同班同學，但真正了解你卻是在研究所的階段；每次有事麻煩你，你總是義無反顧的幫忙。我會珍惜這份友誼，也祝你服研發替代役的日子順利。謝謝在我碩士生涯尾聲出現的小天使—忻恩，因為妳的出現，才讓我在博士班一切順利無懼任何挑戰；有妳的照顧與陪伴，我才能在人生的道路全心全力勇往直前。

最後，要感謝我生命中最重要的家人。感謝父母對我的栽培，讓我的求學過程一路順遂。我努力的想讓您們以我為榮，報答您們的養育之恩。能做您們的孩子，是我這輩子最大的福氣。也要謝謝小舅舅蔡銘昌博士，在我求學的過程中總是支持我，給我許多指點與建議。然後，我想要告訴奶奶，來不及讓您看到我碩士畢業，但您永遠活在我心裡。

這篇論文的完成是我生命中重要的一頁，僅將此篇論文獻給曾經幫助過我的人們。

摘要

近年來，近場通訊系統的應用日趨廣泛，諸如超高頻近場射頻辨識系統、近距離無線通訊技術(NFC)。在近場通訊系統中，我們希望成功的設計天線，並優化系統的效能，因此收發兩端的天線耦合分析就變得很重要。本論文提出一個簡單的公式，可以計算近場通訊系統中傳送天線和接收天線之間的功率耦合係數(power coupling coefficient)。此公式的適用性不拘天線的種類、形式、尺寸、工作頻率；所需的資訊為收發兩端天線在該工作頻率下的三維遠場場形、天線之間的相對傾斜角度及距離。換言之，我們所提出的公式可視為遠場福利斯傳輸方程式(Friis transmission equation)在近場的類比。

為了驗證公式的準確性，我們先考慮幾種常用的天線，利用他們的場形標準式(close-form pattern)，將計算的近場耦合係數和全波分析模擬(HFSS)作比較。此外，我們也以超高頻近場射頻辨識系統為例，設計符合此應用的天線，並且比較量測、模擬、理論計算的結果。透過這些驗證，我們確認所提出的公式可以精準的算出近場功率耦合係數。在實驗中我們也發現了一些影響耦合程度的參數，諸如接收天線的阻抗匹配、發送天線的指向性。藉由提出的公式，我們還可以計算超高頻近場射頻辨識系統的讀取距離以及可靠度。因此，這篇論文提出的成果相信有助於應用在近場通訊系統。

關鍵詞 — 電磁耦合、近場、能量傳輸、射頻辨識、超高頻天線。

Abstract

Recently, near-field communication systems have been widely used in many applications such as the near-field UHF RFID item-level tagging, the Near Field Communication (NFC) device, and the mCoupons. To successfully design and optimize the near-field communication systems, it is important to investigate the near-field coupling between the transmitting and receiving antennas. In this thesis, a simple formula has been presented for computing the coupling coefficient between two antennas that are placed in the near field of each other. The choices of the two antennas are arbitrary, and all the information needed includes the corresponding normalized vector far-field patterns along with their relative orientations and the antenna spacing.

To verify the proposed formulation, the coupling coefficients in several near-field scenarios, including a practical near-field UHF RFID system, are computed and compared to those measured and full-wave simulated using Ansoft HFSS. They are all in good agreement. Additionally, it is shown that several factors may influence the coupling coefficient, such as the impedance matching of the receiving antenna and the directivity of the transmitting antenna. With the aid of the proposed formulation, the near-field read range and read reliability can be determined and the near-field coupling phenomena can be investigated. The results thus obtained may be useful in the near-field communication systems.

Keywords — Electromagnetic coupling, near field, power transmission, RFID, UHF antennas.

Contents

Abstract **I**

Contents **III**

List of Figures **V**

List of Tables **VII**

Chapter 1 Introduction **1**

1.1 Motivation.....1

1.2 Thesis Overview.....3

Chapter 2 Near-Field Coefficient **5**

2.1 Introduction…….....5

2.2 Antenna Field Region…….....6

2.3 Antenna Coupling versus Longitudinal Displacement.....7

2.3.1 Spherical Wave Expansions for the Coupling Coefficient.....9

2.3.2 Evaluation of the Spherical Wave Coefficients.....12

2.3.3 Relative Orientations.....14

2.4 Antenna Coupling versus Transverse Displacement….....15

2.5 Summary…….....17

Chapter 3 Comparisons between the Formulation and HFSS Simulation **19**

3.1 Introduction.....19

3.2 Side-by-Side, Parallel Half-Wave Dipoles.....19

3.3 Side-by-Side, Polarization-Mismatched Half-Wave Dipoles.....22

3.4 Polarization-Matched Square Loop and Half-Wave Dipole.....23

3.5 Summary.....26

Chapter 4 Application in Near-Field UHF RFID System **27**

4.1 Introduction…….....27

4.2 Reader Antenna…….....30

4.3 Tag Antennas…….....34

4.3.1 Folded Dipole with a Closed Loop…….....34
4.3.2 Meander Circular Loop.....37
4.3.3 Microstrip-to-CPS Transition.....39
4.4 Measurement Results…….....41
4.4.1 Coupling Coefficient versus Longitudinal Displacement.....43
4.4.2 Coupling Coefficient versus Transverse Displacement.....45
4.5 Enhancement of Power Coupling Level…….....51
4.5.1 Impedance Matching of the Receiving Antenna…….....51
4.5.2 Directivity of the Transmitting Antenna…….....54
4.6 Practical Applications of Near-Field RFID Systems.....55
4.6.1 Near-Field Read Range……..…….....55
4.6.2 Read Reliability…….....57
4.7 Summary…….....60

Chapter 5 Conclusions 61
5.1 Summary of This Thesis……....……..…….....61
5.2 Future Works…….....……....62

Appendix 65
A.1 Coupling Quotient in Terms of Far-Field Patterns…….....65
A.2 Series Expansions of Spherical Wave Functions…….....67
A.3 Orthogonality Relationship of Tesseral Harmonics…….....70

References 73

List of Figures

Chapter 2 Near-Field Coupling Coefficient 5

Fig. 2-1 Antenna near and far field regions.....7

Fig. 2-2 Arbitrarily oriented receiving antenna in the near field of a transmitting antenna…….....8

Fig. 2-3 Rotated (primed) coordinate system with receiving antenna on the z'-axis.....11

Fig. 2-4 A relative orientation of the receiving antenna in terms of spherical coordinate system….....15

Fig. 2-5 The receiving antenna has an offset on the transverse plane normal to the separation axis….16

Chapter 3 Comparisons between Formulation and Simulation 19

Fig. 3-1 Geometry of the HFSS simulated dipole.....20

Fig. 3-2 Simulated radiation patterns of the dipole at 915MHz
(a) x-z plane and (b) y-z plane.....21

Fig. 3-3 Coupling coefficient versus antenna separation for polarization-matched dipoles……..21

Fig. 3-4 Coupling coefficient versus antenna separation for polarization-mismatched dipoles……....23

Fig. 3-5 Geometry of the HFSS simulated square loop.....24

Fig. 3-6 Simulated radiation patterns of the square loop antenna at 915MHz
(a) x-z plane and (b) y-z plane.....24

Fig. 3-7 Coupling coefficient versus antenna separation for polarization-matched square loop and dipoles.....25

Chapter 4 Application in Near-Field UHF RFID System 27

Fig. 4-1 Simplified architecture of near-field RFID systems.....29

Fig. 4-2 Geometry of two-element square loop array with a back reflector…….…….31

Fig. 4-3 Photographs of two-element square loop array with a back reflector.....31

Fig. 4-4 Simulated and measured input return losses of the reader antenna.....32

Fig. 4-5 Simulated and measured radiation patterns of the proposed reader antenna at 920MHz
(a) x-z plane and (b) y-z plane.....33

Fig. 4-6 Geometry of the folded dipole antenna…….....35

Fig. 4-7 Photograph of the folded dipole antenna…….....35

Fig. 4-8 Simulated and measured return losses of the folded dipole with the Balun.....36

Fig. 4-9 Simulated and measured radiation patterns of the folded dipole with the Balun at 920MHz
(a) x-z plane and (b) y-z plane.....37

Fig. 4-10 (a) Photograph of 930-MHz meander loop
(b) Geometry of meander loop fed by CPS and balun.....38

Fig. 4-11 Simulated and measured return losses of the meander loop with the Balun.....38

Fig. 4-12 Simulated and measured radiation patterns of the meander loop with the Balun at 930MHz (a) x-z plane and (b) y-z plane.....39
Fig. 4-13 Proposed structure of the microstrip-to-CPS transition.....40
Fig. 4-14 Measurement setup for the near-field RFID system…….....42
Fig. 4-15 Photograph of HP8753D VNA.....42
Fig. 4-16 Photograph of the measurement setup in anechoic chamber.....43
Fig. 4-17 Coupling coefficient versus antenna separation for the near-field RFID setup at 920 MHz (Tag antenna: folded dipole).....44
Fig. 4-18 Coupling coefficient versus antenna separation for the near-field RFID setup at 930 MHz (Tag antenna: meander circular loop).....45
Fig. 4-19 Photographs of (a) the reader antenna which is fixed at a certain position, and (b) the tag antenna which is located on a near-field planar scanner.....46
Fig. 4-20 Coupling coefficient versus transverse displacements for *d* = 100 mm (a) Calculated and (b) measured 3D surface plots (c) calculated and (d) measured contour plots.....48
Fig. 4-21 Coupling coefficient versus transverse displacements for *d* = 200 mm (a) Calculated and (b) measured 3D surface plots (c) calculated and (d) measured contour plots.....49
Fig. 4-22 Coupling coefficient versus transverse displacements for *d* = 300 mm (a) Calculated and (b) measured 3D surface plots (c) calculated and (d) measured contour plots.....50
Fig. 4-23 Photograph of the curve of $|S_{21}|^2$ on the VNA.....52
Fig. 4-24 Coupling coefficient versus antenna separation for the near-field RFID setup at 910, 920, 930, and 940 MHz. (Tag antenna: folded dipole).....53
Fig. 4-25 Coupling coefficient versus antenna separation for the near-field RFID setup at 910, 920, 930, and 940 MHz. (Tag antenna: meander circular loop).....53
Fig. 4-26 Coupling coefficient versus antenna separation for the near-field RFID setup at 920 MHz (Tag antenna: folded dipole. Reader antenna: meander circular loop and square loop array with back reflector.....54
Fig. 4-27 Geometry of the basket which is 10 cm above the reader antenna.....59
Fig. 4-28 Comparison of simulated and measured CDF of read reliabilities at 930 MHz (Tag antenna: meander circular loop. Reader antenna: square loop array with back reflector)……...59

List of Tables

Chapter 4 Application in Near-Field UHF RFID System 27

Table 4.1 Comparison between the simulation and measurement.....58

Chapter 1

Introduction

1.1 Motivation

In the past years, there have been increasing research interest in near-field communication systems, and the emerging technology has been deployed in many diverse applications. For example, the near-field UHF RFID has been used in item-level tagging such as pharmaceutical and retailing [1]-[3]. The LF and HF RFID systems have been extensively used in the access control and public transportation ticketing. The Near Field Communication (NFC) system that enables contactless payments via any hand-held device, say a mobile phone, also receives considerable attentions [4]-[6]. There are still other applications, such as the health monitoring [7], the mCoupons [8], and the magnetic resonance imaging (MRI) [9], etc.

In order to successfully design and optimize the near-field communication systems, it is critical to investigate the antenna coupling between transmitting and receiving antennas that are placed in the near zone of each other. In lower frequency range, such as the LF (125-134 KHz) and the HF (13.56 MHz) bands, either the electric field or magnetic field would dominate in the antenna near zone depending on the antenna type. The electric field of an electric dipole antenna dominates, whereas the magnetic field of

an electric loop antenna dominates. Therefore, in the near-field magnetic (inductive) coupling system, the transmitting and receiving antennas used are mostly loop antennas. Some attempts have been made to compute the LF/HF inductive coupling power transfer [10]-[13]. However, in the UHF band or even higher, such as the 860-960 MHz, 2.4-GHz, and 5.8-GHz bands, inductive and capacitive coupling are associated with different regions of the antenna impedance. The field distribution in the same near zone becomes more complicated and may also include an electrostatic or magnetostatic component. While an antenna radiates the electromagnetic field, the near-field region can be either inductive or capacitive which relying upon the operating frequency. To the authors' best knowledge few studies have so far been done on emphasizing the generality for any antenna types and the relative orientation of the antennas for calculating the near-field antenna coupling in the microwave region.

The goal of this thesis is to propose an analytic form to compute the near-field coupling coefficient as a function of the spacing between two arbitrary antennas. In near-field measurement, we can determine the far-field pattern of antenna by measuring the near-field coupling between test and probe antennas [14]. The proposed formulation, in a sense, is an inverse transformation of near-field measurements. We can calculate the near-field coupling coefficient by means of the three-dimensional vector far-field patterns and the relative orientation of the transmitting and receiving antennas. The

proposed formulation is a near-field counterpart of the Friis equation in the far zone, and is applicable to any antennas used in the near-field communication systems.

1.2 Thesis Overview

This thesis is organized as below. **Chapter 2** presents the formulation to calculate the near-field coupling coefficient. It is based mainly on the coupling quotient expressed in terms of the antenna far fields [15]. However, the associated numerical complexity due to the usage of the fast Fourier transform (FFT) and the tedious truncation methods has been greatly reduced.

For verification, the formula is used to calculate the coupling coefficients of several near-field setups. In **Chapter 3**, three commonly-seen scenarios are simulated using Ansoft HFSS. The results are compared with those computed via the proposed method, and they agree well.

In **Chapter 4**, a near-field UHF RFID system is chosen as an example. All the results obtained through measurement, HFSS simulation, and the formulation are demonstrated and compared. Some factors are found and discussed for enhancing the coupling level. Additionally, several practical applications in near-field UHF RFID systems are performed, and the proposed formulation may be helpful for determining the near-field read range and read reliability.

Finally, some observations and design guidelines are summarized in **Chapter 5**. Three Appendices are attached at the end of this thesis. The derivation of coupling quotient in terms of far-field patterns is shown in Appendix 1. The general solution of the scalar Helmholtz equation in spherical coordinates is derived in Appendix 2. Moreover, in Appendix 3, it derives the orthogonality relationships of tesseral harmonics.

Chapter 2

Near-Field Coupling Coefficient

2.1 Introduction

In wireless communication, it's crucial to determine the coupling coefficient, that is, the amount of power accepted by the receiving antenna when a given amount of power comes from the transmitting antenna. When the receiving antenna is located in the far field of the transmitting antenna, the coupling coefficient can be determined by the Friis equation:

$$C = G_t G_r \left(\frac{\lambda}{4\pi d} \right)^2 p \tag{2.1}$$

where G_t, G_r are the gains of transmitting and receiving antennas, respectively, d is the antenna spacing, and p is the polarization mismatch loss between the two antennas. As for the near-field case, in order to determine the coupling coefficient between the transmitting and receiving antennas, we require other approaches described in this chapter. We have organized this part into following sections. In Section 2.2, we categorize the exterior fields of the transmitting antenna, and clarify the near-field region considered in this thesis. Section 2.3 presents the theory for computing the coupling coefficient versus longitudinal displacement of two antennas separated along axis, which is considered as the prototype of the three-dimensional formulation. Since

the transmitting and receiving antennas are often randomly oriented, we merge the orientation obstacle into the formulation described in subsection 2.3.3. Furthermore, the coupling coefficient versus relative displacement of two antennas in a transverse plane normal to the separation axis is also discussed in Section 2.4. Finally, the capability of the formulation is summarized in Section 2.5.

2.2 Antenna Field Regions

The exterior fields of a transmitting antenna can be divided into near-field and far-field regions as shown in Fig. 2.1 [14], [19]. The near-field region is further divided into two sub-regions, the reactive and radiating near field. In the reactive near field, energy is stored in the electric and magnetic fields very close to the transmitting antenna instead of radiating from the source. The near-field region is commonly taken to extend about $\lambda/2\pi$ from the surface of the antenna. However, with the experience of near-field measurement, it indicates that a distance of one wavelength (λ) determines a more reasonable outer boundary to the reactive near field. Once the distance from the transmitting antenna is more than one wavelength, the electric and magnetic fields tend to propagate predominantly in phase, but do not exhibit a plane-wave characteristic ($\exp(ikr/r)$) until they reach the far-field region. This propagation region between the reactive near field and the far field is called the radiating near field.

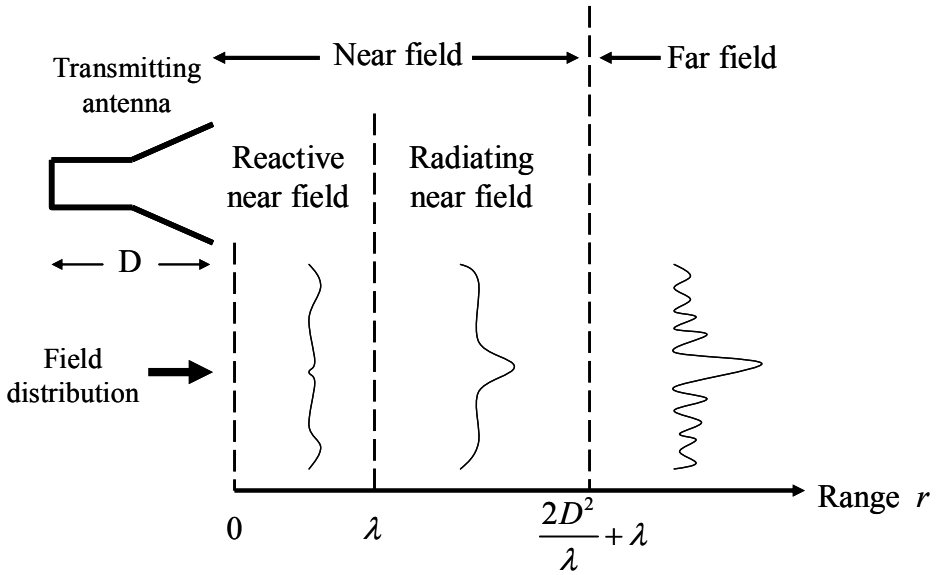

Fig. 2.1 Antenna near and far field regions.

The far-field region extends to infinity and the direction of electric field, magnetic field and propagation are perpendicular among one another in this region. The inner radius of the far field can be estimated from the general free-space integral for the vector potential and is typically set at $2D^2/\lambda+\lambda$. Notice that the added λ covers the possibility of the maximum dimension D of the antenna being smaller than a wavelength. In other words, the so-called Rayleigh distance $2D^2/\lambda$ is measured from the outer boundary of the reactive near field of the antenna.

2.3 Antenna Coupling versus Longitudinal Displacement

Consider a receiving antenna placed in the near field of a transmitting antenna as depicted in Fig. 2.2. The incident and emergent waveguide mode coefficients for the transmitting (receiving) antenna are a_T and b_T (a_R and b_R) respectively. Referring to [15],

the coupling quotient between the transmitting and receiving antennas is defined as b_R/a_T. It can be interpreted as the signal coupled into the receiving antenna when a unit signal is fed into the transmitting antenna, which is identical to the definition of the forward transmission coefficient of the scattering parameters S_{21}, when the transmitting and receiving antennas and the region in between are considered as a two-port network.

Since we are more interested in the coupled power level, $|b_R/a_T|^2$ is used instead. It means the amount of power accepted by the receiving antenna when a unit power comes from the transmitting antenna. Mostly, $|b_R/a_T|^2$ is expressed in decibels and is referred to as the **power coupling level** or the **coupling coefficient *C*** here in this thesis.

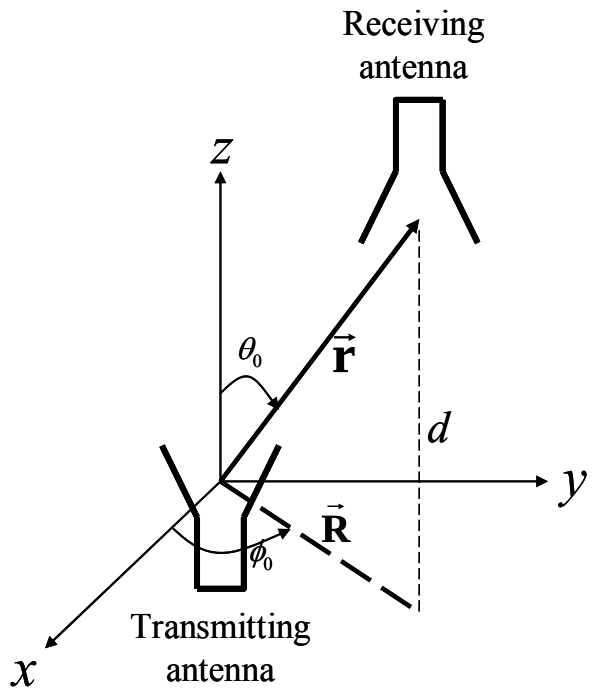

Fig. 2.2 Arbitrarily oriented receiving antenna in the near field of a transmitting antenna.

2.3.1 Spherical Wave Expansions for the Coupling Coefficient

The coupling quotient between the transmitting and receiving antennas can be written as [15]

$$\frac{b_R}{a_T} = -\frac{C_R}{k} \iint_{K<k} \frac{f_R(-\mathbf{k}) \cdot f_T(\mathbf{k})}{k_z} e^{i\mathbf{k}\cdot\mathbf{r}} dk_x dk_y \tag{2.2}$$

where $\mathbf{k} = \hat{x}k_x + \hat{y}k_y + \hat{z}k_z$ is the propagation vector, and $k = |\mathbf{k}| = 2\pi/\lambda$ with λ the free-space wavelength. $\mathbf{r} = \hat{x}x + \hat{y}y + \hat{z}d = \mathbf{R} + \hat{z}d$ is the position vector of the receiving antenna with respect to the transmitting antenna. $f_R = \hat{\theta}f_{R\theta} + \hat{\phi}f_{R\phi}$ and $f_T = \hat{\theta}f_{T\theta} + \hat{\phi}f_{T\phi}$ are the normalized vector far-field patterns for the receiving and transmitting antennas, respectively. C_R is a mismatch constant defined as

$$C_R = \frac{Z_{RFeed}}{\eta(1 - \Gamma_R \Gamma_L)} \tag{2.3}$$

where η is the intrinsic impedance of free space, Z_{RFeed} is the characteristic impedance of the feed waveguide of the receiving antenna, and Γ_R, Γ_L are the reflection coefficients of the feed waveguide when looking into the receiving antenna and its passive load, respectively. The derivation of (2.2) is done by Yaghjian [15] and shown in Appendix 1.

Note from (2.2) that the coupling quotient is a function of the position vector **r**. The double integral in (2.2) is taken over the transverse components of propagation vector dk_x and dk_y, and the inner product of the two vector far-field patterns in the integrand represents the interaction between the transmitting and receiving antennas.

The integral interval $K < k$ means that only the propagating waves are integrated, which corresponds to the real part of the complex power.

Applying the Laplacian operator ∇^2 to (2.2) yields

$$\begin{aligned}\nabla^2 \frac{b_R}{a_T} &= -\frac{C_R}{k} \iint_{K<k} \frac{f_R(-\mathbf{k}) \cdot f_T(\mathbf{k})}{k_z} \left[\nabla^2 e^{i\mathbf{k}\cdot\mathbf{r}} \right] dk_x dk_y \\ &= -\frac{C_R}{k} \iint_{K<k} \frac{f_R(-\mathbf{k}) \cdot f_T(\mathbf{k})}{k_z} \left(-k^2\right) e^{i\mathbf{k}\cdot\mathbf{r}} dk_x dk_y\end{aligned} \tag{2.4}$$

Recasting (2.4) and we have

$$\left(\nabla^2 + k^2\right) \frac{b_R}{a_T} = 0 \tag{2.5}$$

which means that the coupling quotient satisfies the scalar Helmholtz equation. As a result, the coupling quotient can be expanded by linear combination of the elementary wave functions, and the most general form is a summation over all possible values of m and n [16], written as (see Appendix 2)

$$\frac{b_R}{a_T} = \sum_{n=0}^{\infty} \sum_{m=-n}^{n} B_{nm} h_n^{(1)}(k\mathbf{r}) P_n^m(\cos\theta_0) e^{im\varphi_0} \tag{2.6}$$

where r, θ_0, and ϕ_0 are the corresponding spherical coordinates of the position vector $\mathbf{r}$. $h_n^{(1)}$ and P_n^m are the spherical Hankel functions of the first kind and the associated Legendre polynomials, respectively. B_{nm} are the spherical wave coefficients. Here, the coupling quotient is expanded by a set of known basis which can be determined by forward recurrence relations or obtained in Matlab and Mathematica databases, and leaving only the spherical wave coefficients B_{nm} unknown.

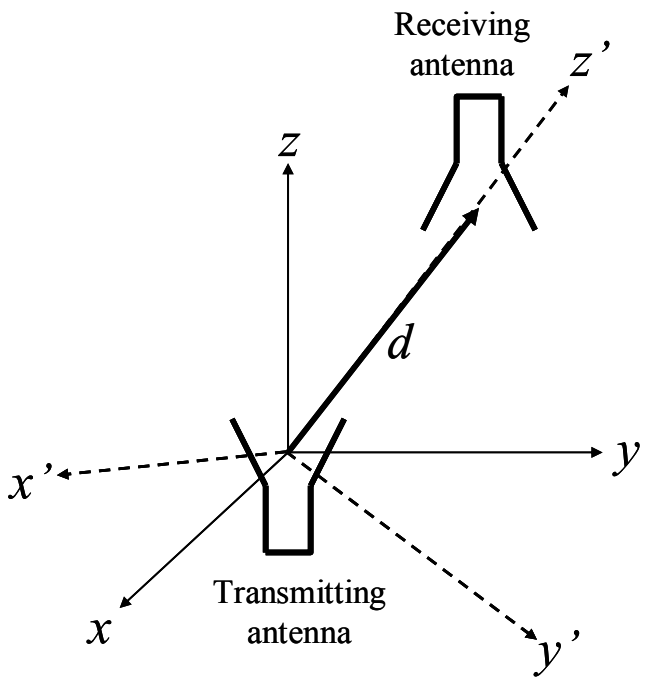

Fig. 2.3 Rotated (primed) coordinate system with receiving antenna on the z'-axis.

Through the above series expansion method, the singularity that occurs when γ approaches zero can be avoided, and the integration variables dk_x and dk_y are changed to be $d\theta_0$ and $d\phi_0$, resulting in a simpler double integral. To further simplify (2.6) and facilitate evaluation of B_{nm}, the coordinate system in Fig. 2.2 is rotated around the origin, namely the phase center of the transmitting antenna, such that the phase center of the receiving antenna lies on the z-axis of the rotated coordinate system as depicted in Fig. 2.3.

Therefore, in this new coordinate system $\mathbf{r} = \hat{z}d$ and θ_0 = 0°. The relative orientation between the transmitting and receiving antennas can then be accounted for simply by rotating the far-field patterns accordingly. In addition, it is known that the

associated Legendre polynomial $P_n^m(\cos\theta_0)$, for its argument being unity, is nonzero only when $m = 0$. Thus (2.6) can be rewritten as (2.7):

$$\frac{b_R}{a_T} = \sum_{n=0}^{\infty} B_n h_n^{(1)}(kd), \qquad d > \frac{D_T + D_R}{2} \tag{2.7}$$

where D_T and D_R are the largest dimensions of the transmitting and receiving antennas, respectively. The coupling quotient in (7) is now a function of the antenna spacing d rather than the position vector **r**. The remaining work is to evaluate the unknown spherical wave coefficients B_{nm} and B_n.

2.3.2 Evaluation of the Spherical Wave Coefficients

To evaluate B_{nm} and acquire B_n in (2.7), first we begin with (2.2), and let the separation distance r approach to infinite. According to the Sommerfeld radiation condition, (2.2) can be written as

$$\frac{b_R}{a_T}(r) \underset{r\to\infty}{\sim} \frac{2\pi C_R i}{k} f_R(-\mathbf{k}) \cdot f_T(\mathbf{k}) \frac{e^{ikr}}{r} \tag{2.8}$$

On the other hand, as $r \to \infty$ the spherical Hankel function in (2.6) has an approximation of large arguments [17] and behaves as

$$h_n^{(1)}(kr) \underset{r\to\infty}{\sim} (-i)^{n+1} \frac{e^{ikr}}{kr} \tag{2.9}$$

Substituting (2.9) into (2.6), and compared with (2.8), we have

$$\frac{b_R}{a_T}(r)\underset{r\to\infty}{=}2\pi C_R i\times f_R(-\mathbf{k})\cdot f_T(\mathbf{k})\times\frac{e^{ikr}}{kr}$$
$$=\sum_{n=0}^{\infty}\sum_{m=-n}^{n}B_{nm}\left[(-i)^{n+1}\frac{e^{ikr}}{kr}\right]P_n^m(\cos\theta_0)e^{im\phi_0} \tag{2.10}$$

Clearly ,e^{ikr}/kr can be canceled out. In a further step, we multiply both side of (2.10) by $P_n^m(\cos\theta_0)e^{-im\phi_0}$, and exploit the orthogonality relationships of those basis functions as shown by Appendix 3, we have

$$B_{nm}=-C_R\frac{i^n(2n+1)}{2}\frac{(n-m)!}{(n+m)!}\times$$
$$\int_0^{\pi}\int_0^{2\pi}f_R(-\mathbf{k})\cdot f_T(\mathbf{k})P_n^m(\cos\theta_0)e^{-im\phi_0}\sin\theta_0 d\phi_0 d\theta_0 \tag{2.11}$$

For m = 0, (2.11) reduces to

$$B_n=B_{n0}=-C_R\frac{2n+1}{2}(i)^n\times$$
$$\int_0^{\pi}\int_0^{2\pi}f_R(-\mathbf{k})\cdot f_T(\mathbf{k})P_n^0(\cos\theta_0)\sin\theta_0 d\phi_0 d\theta_0 \tag{2.12}$$

Given the 3D vector far-field patterns for both transmitting and receiving antennas and the relative orientation, the associated inner product in the integrand of (2.12) could readily be calculated. Please note that to evaluate B_n Yaghjian exploited an FFT algorithm in [14] to convert the double integral into summations. In this work, a simple numerical integration is adopted to calculate B_n directly from (2.12). Substituting B_n thus obtained into (2.7) yields the desired coupling quotient. Although an infinite series is needed based on (2.7) to compute the coupling quotient, it has been observed that the series would converge with merely less than ten terms.

Furthermore, in the far-field Friis equation (2.1) $p = \left|\hat{e}_t \cdot \hat{e}_R\right|^2$ indicates the polarization mismatch loss between two antennas, where $\hat{e}_t$ and $\hat{e}_R$ are unit vectors representing the polarization of the electric field of the transmitting and receiving antennas, respectively. In the proposed near-field formulation, the polarization mismatch loss has also been consulted by the pattern inner product $f_R \cdot f_T$ since we can always express f_R as $\hat{\theta} f_{R\theta} + \hat{\varphi} f_{R\varphi}$ and f_T as $\hat{\theta} f_{T\theta} + \hat{\varphi} f_{T\varphi}$. Consequently, the proposed formulation, in a sense, can be regarded as a near-field counterpart of the Friis transmission formula.

2.3.3 Relative Orientations

To evaluate the inner product $f_R \cdot f_T$, the normalized far-field vector patterns(f_R and f_T) are transferred from the spherical coordinate system to the rectangular coordinate system. Since there is often a relative orientation between transmitting and receiving antennas, consider each antenna rotates about Z-axis as illustrated in Fig. 2.4. We convert f_ϕ, f_θ from spherical coordinates into f_x, f_y, f_z in rectangular coordinates by

$$\begin{bmatrix} f_x \\ f_y \\ f_z \end{bmatrix} = \begin{bmatrix} -\sin\phi_A & \cos\theta_A \cos\phi_A \\ \cos\phi_A & \cos\theta_A \sin\phi_A \\ 0 & -\sin\theta_A \end{bmatrix} \begin{bmatrix} f_\phi \\ f_\theta \end{bmatrix} \tag{2.13}$$

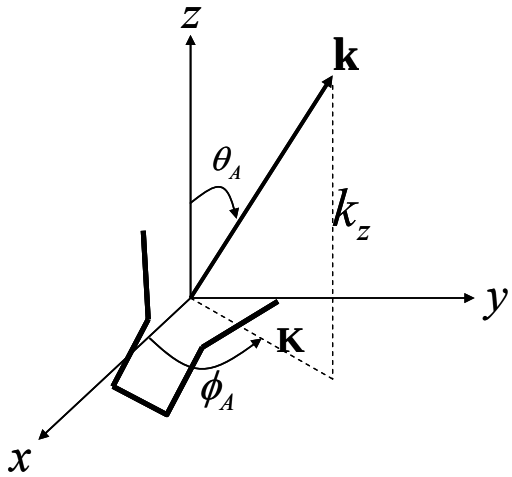

Fig. 2.4 A relative orientation of the receiving antenna in terms of spherical coordinate system (θ_A, ϕ_A).

After obtaining f_x, f_y, f_z, we can substitute it into (2.12) to compute the pattern inner product, and further attain (2.7).

2.4 Antenna Coupling versus Transverse Displacement

In the preceding work, we evaluate the coupling coefficient versus the longitudinal axis between the transmitting and receiving antenna. Mostly, in this situation the coupling coefficient is larger than the scenario that the receiving antenna has an offset (Δx, Δy) on a transverse plane and is separated from the transmitting antenna by d. Typically this scenario is often our concern for application purpose.

The coupling coefficients are also obtained for this scenario. Consider the transmitting antenna is located at the coordinate origin, while the receiving antenna "scans" on a transverse plane with a constant antenna orientation. Fig. 2.5 shows the

receiving antenna located at an off-axis point A' with transverse offsets (Δx, Δy) from the on-axis point A. The transverse offsets can then be converted into the relative orientation for the antennas.

$$\begin{cases} \Delta\phi = \tan^{-1}\left(\dfrac{\Delta y}{\Delta x}\right) \\ \Delta\theta = \tan^{-1}\left(\dfrac{\sqrt{\Delta x^2 + \Delta y^2}}{d}\right) \end{cases} \tag{2.14}$$

Given the tag antenna position A'(Δx, Δy, d) and the 3D patterns of the reader and tag antennas, the associated coupling coefficient can be computed by rotating the 3D patterns in accordance with the relative antenna orientation. Also, note that the antenna spacing in the formula should be d' instead of d.

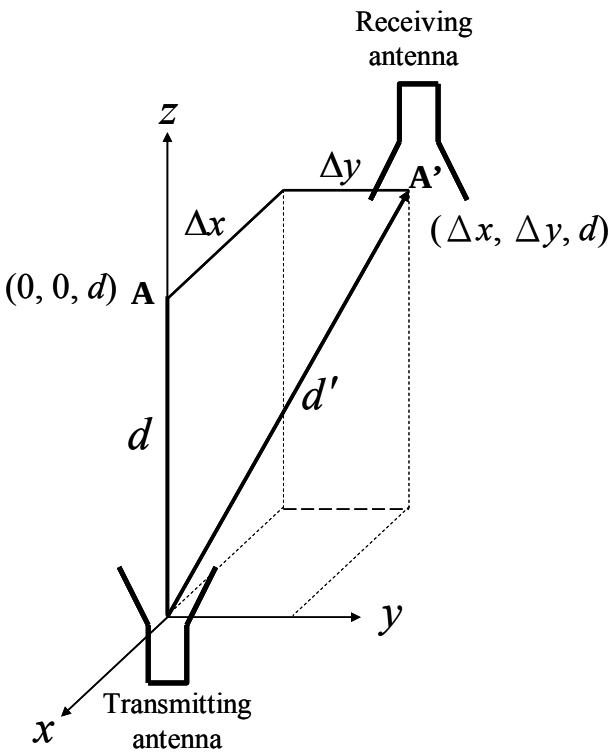

Fig. 2.5 The receiving antenna has an offset (Δx, Δy) on the transverse plane normal to the separation axis.

2.5 Summary

In this chapter, we specify the near-field region discussed in this thesis. A simple formulation has been presented for computing the coupling coefficients between two antennas that are placed in the near field of each other and are arbitrarily oriented. Although the formula is complicated to some extent, it could be regarded as a near-field counterpart of the Friis transmission formula. Based on the proposed formula and program, all the information we need to compute the near-field coupling coefficient are the 3D radiation patterns of each antenna and their relative orientation.

Chapter 3

Comparisons between the Formulation and HFSS Simulation

3.1 Introduction

In order to verify the proposed formulation, three classic scenarios in the UHF band are considered in this chapter. The design frequencies of all the antennas are at 915 MHz. The associated coupling coefficients between the transmitting and receiving antennas are computed and compared to those simulated using Ansoft HFSS. Please note that, in the HFSS simulation, the quantity $|S_{21}|^2$ is used for comparison, which is obtained by assuming port 2, namely the receiving antenna in our cases, being perfectly matched to its load impedance. For consistency, this condition can be included in our formulation merely by setting $\Gamma_{RL} = 0$. Also, it must be mentioned that according to the condition in (2.7) the coupling coefficients can be computed only when the antenna separation is larger than the mean value of the largest dimensions for the transmitting and receiving antennas. Therefore, $d \geq 85$ mm is chosen in the following examples.

3.2 Side-by-Side, Parallel Half-Wave Dipoles

Consider two identical, y-directed half-wavelength dipole antennas, one of which is placed at the origin and the other on the z-axis with a separation *d*. The former is

chosen as the transmitting antenna, while the latter is the receiving antenna. Since it is not difficult to derive the normalized vector far-field pattern of an ideal y-directed half-wavelength dipole based on its well-known z-directed counterpart, they are given as

$$f_\theta \propto \frac{\cos\left(\dfrac{\pi \sin\theta \sin\varphi}{2}\right)}{1-\sin^2\theta\sin^2\varphi}\cos\theta\sin\varphi \tag{3.1}$$

$$f_\varphi \propto \frac{\cos\left(\dfrac{\pi \sin\theta \sin\varphi}{2}\right)}{1-\sin^2\theta\sin^2\varphi}\cos\varphi \tag{3.2}$$

Substituting (3.1) and (3.2) into (2.12) yields the desired spherical wave coefficients B_n. The computed coefficients B_n diminishes significantly for higher order terms when $n > 7$ leading to fast convergence of (2.7). In the HFSS simulation, the configuration of the dipole is shown in Fig 3.1, and the corresponding patterns at 915 MHz are shown in Fig 3.2.

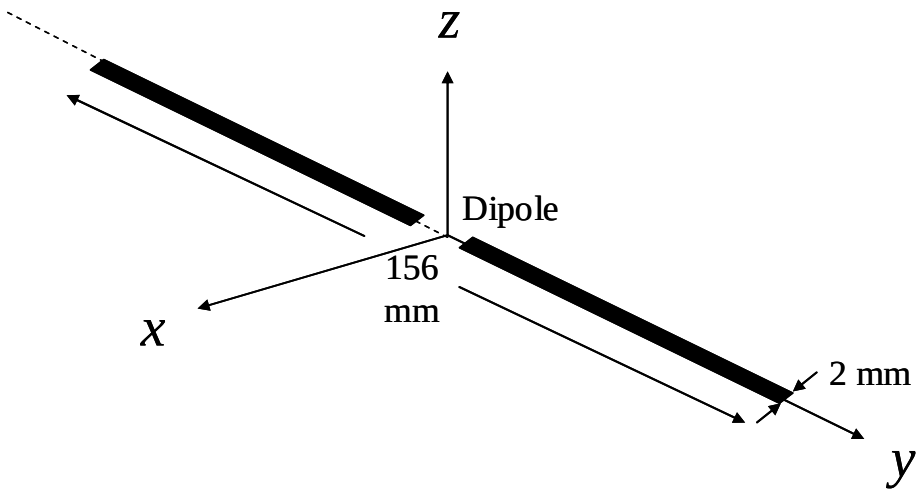

Fig. 3.1 Geometry of the HFSS simulated dipole.

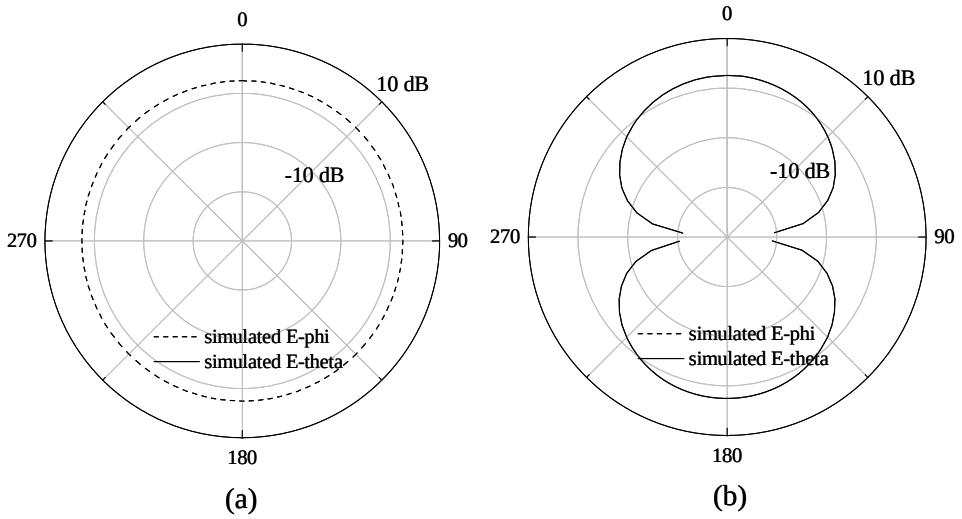

Fig. 3.2 Simulated radiation patterns of the dipole at 915MHz.
(a) x-z plane and (b) y-z plane.

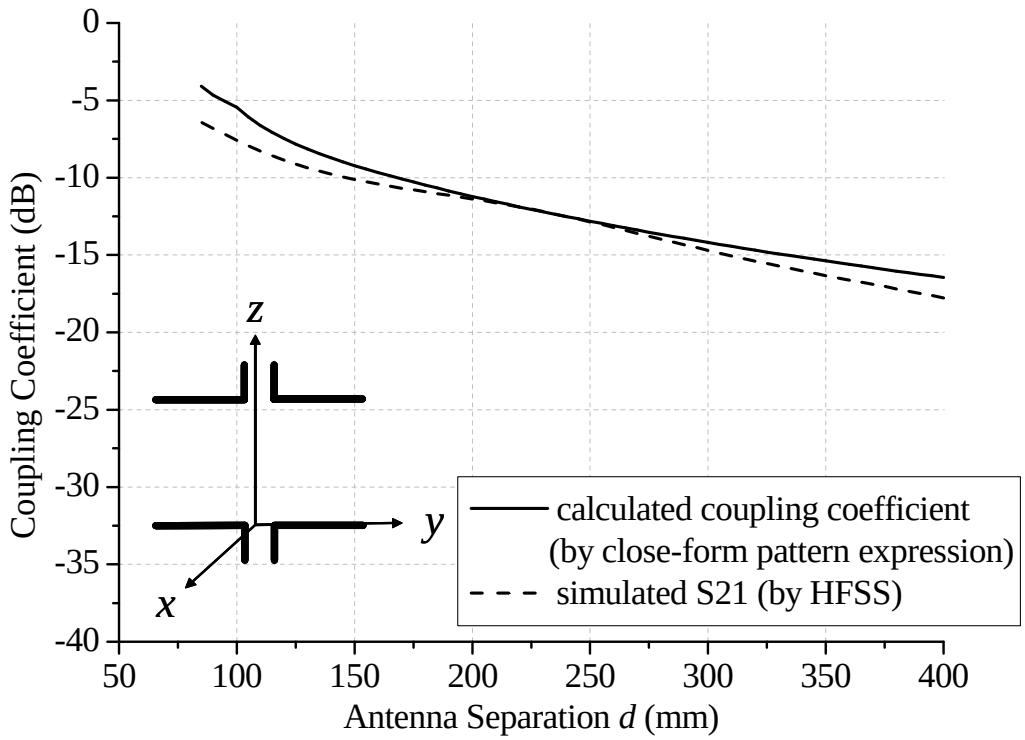

Fig. 3.3 Coupling coefficient versus antenna separation for polarization-matched dipoles.

The near-field coupling coefficient as a function of antenna spacing *d* computed by the proposed method and those obtained via HFSS are depicted in Fig. 3.3. Excellent agreement can be observed verifying the proposed formulation.

3.3 Side-by-Side, Polarization-Mismatched Half-Wave Dipoles

In the preceding subsection, the two dipoles are polarization matched corresponding to the best case in a two-dipole system. However, in most cases, they are arbitrarily oriented. Besides, to demonstrate the capability of our method, a scenario having polarization-mismatched dipoles is also considered. In the current case, the receiving dipole lying on the y-z plane is rotated by 20° around its phase center. This can be accounted for in our formulation simply by transforming the coordinate system of the vector far-field pattern of the receiving dipole accordingly. Using (2.13), θ_A and ϕ_A defined in Fig. 2.3 are 20° and 90°, respectively. Accordingly the corresponding rectangular components of the receiving antenna are

$$\begin{cases} f_{xR} = -f_{\phi R} \\ f_{yR} = \cos 20° \cdot f_{\theta R} \\ f_{zR} = -\sin 20° \cdot f_{\theta R} \end{cases} \tag{3.3}$$

Likewise, B_n thus obtained diminishes significantly for $n > 9$ leading to fast convergence of (2.7). The coupling coefficients thus obtained are plotted in Fig. 3.4. One can see that the coupling coefficients are smaller here than in the preceding case because of the polarization mismatch between the two dipoles.

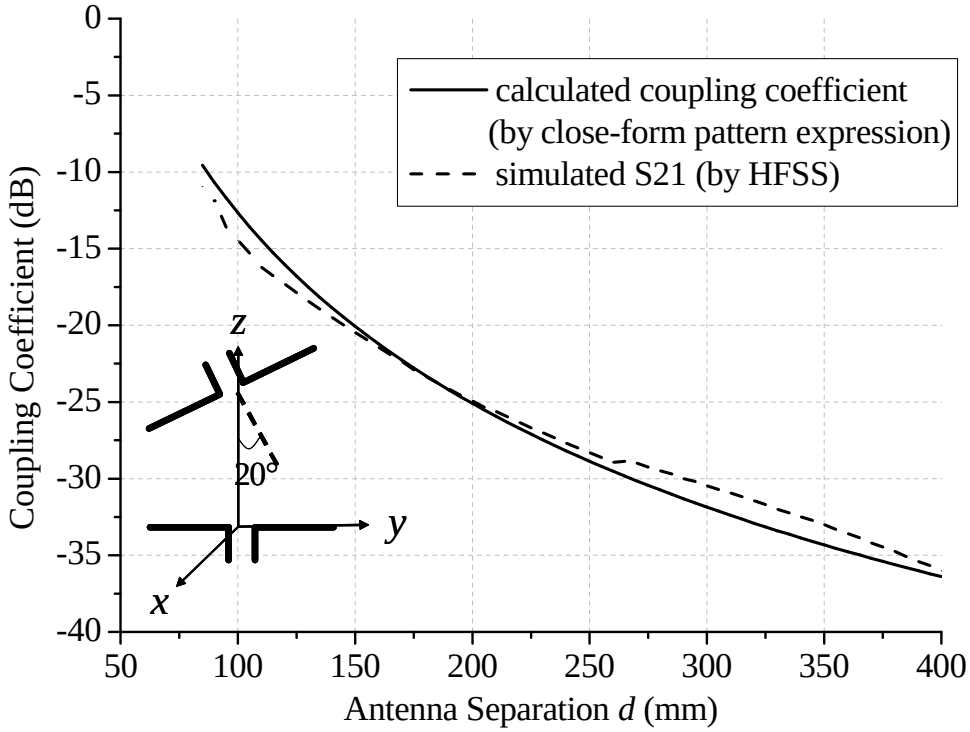

Fig. 3.4 Coupling coefficient versus antenna separation for polarization-mismatched dipoles.

3.4 Polarization-Matched Square Loop and Half-Wave Dipole

Here, a square loop antenna having its perimeter equal to a wavelength is used to replace the transmitting dipole in Section 3.2. The loop antenna is centered at the origin with the loop lying on the x-y plane and oriented in such a way that the resultant polarization is aligned with the y-directed receiving dipole. In the HFSS simulation, the structure of the square loop antenna and the patterns are shown in Fig 3.5 and Fig 3.6, respectively.

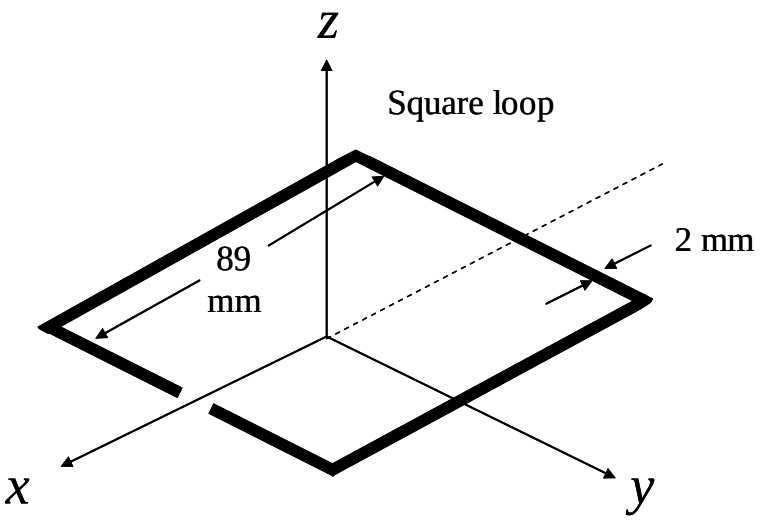

Fig. 3.5 Geometry of the HFSS simulated square loop.

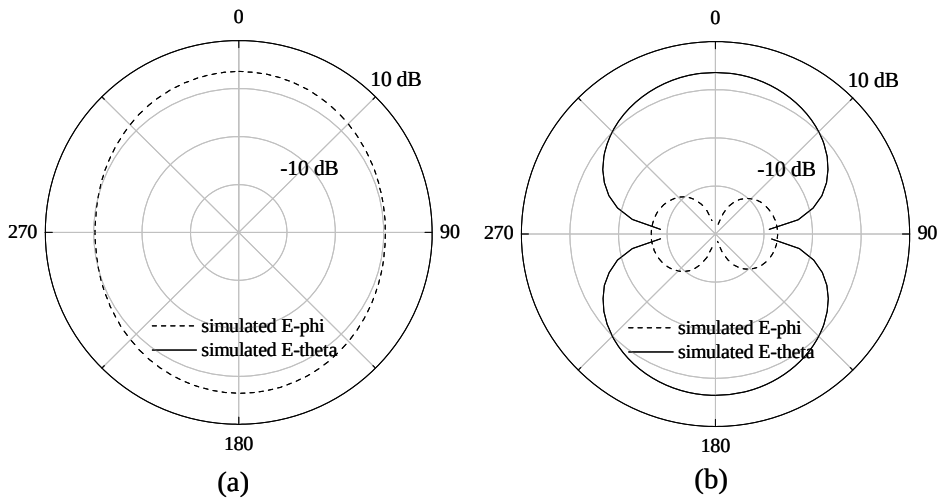

Fig. 3.6 Simulated radiation patterns of the square loop antenna at 915MHz.
(a) x-z plane and (b) y-z plane.

We observe that the simulated pattern in the y-z plane is doughnut-shaped, while the x-z plane pattern is omni-directional with a slightly shaking at ±90°. This circumstance indicates that its normalized co-polarized component of the far-field pattern can be represented as an array composed of two parallel dipoles a quarter wavelength apart. Consequently, the radiation patterns of the square loop can be approximated using the principle of pattern multiplication with the element factor

$$f_\theta \propto \frac{\cos\left(\frac{\pi \sin\theta \sin\varphi}{4}\right) - \cos\frac{\pi}{4}}{1-\sin^2\theta\sin^2\varphi}\cos\theta\sin\varphi \tag{3.4}$$

$$f_\varphi \propto \frac{\cos\left(\frac{\pi \sin\theta \sin\varphi}{4}\right) - \cos\frac{\pi}{4}}{1-\sin^2\theta\sin^2\varphi}\cos\varphi \tag{3.5}$$

while the array factor can be derived as

$$AF = 1 + e^{j\frac{\pi}{2}\sin\theta\sin\phi} \tag{3.6}$$

The coupling coefficient for this setup can thus be computed as a function of the antenna spacing. The results are compared with those simulated and shown in Fig. 3.7. In this example, the error is larger than previous two cases due to the far-field pattern of square loop is an approximation, which is not a exact solution used in previous cases.

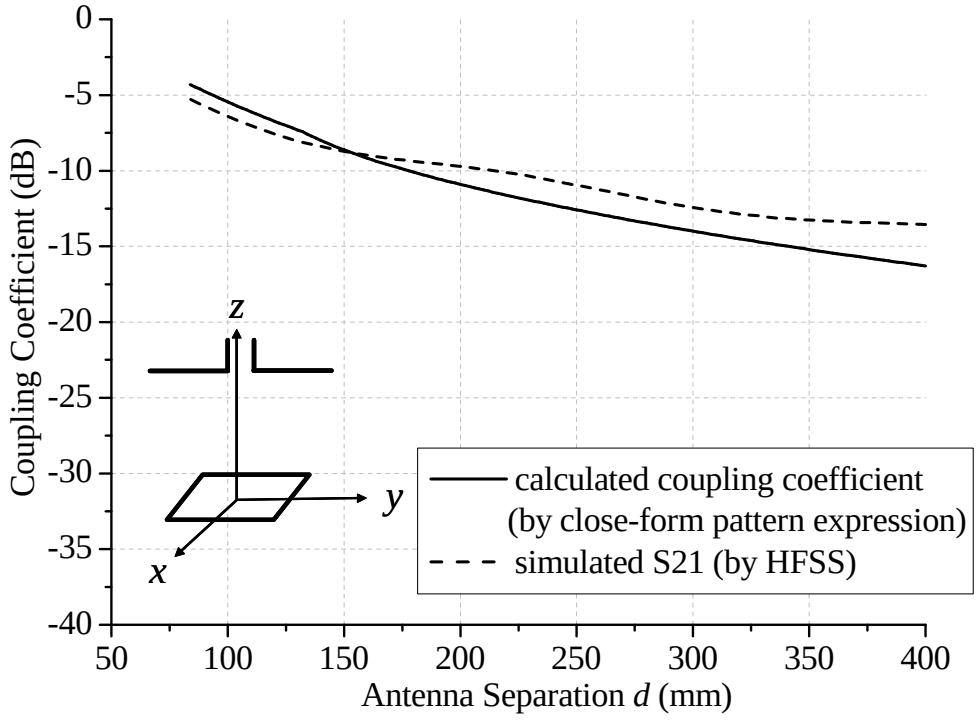

Fig. 3.7 Coupling coefficient versus antenna separation for polarization-matched square loop and dipole.

3.5 Summary

In the previous three scenarios, the agreement between the computed results and those simulated by HFSS indicates that the proposed method can be utilized to determine the near-field coupling coefficient as the relative orientation, the antenna spacing, and the far-field patterns of the transmitting and receiving antennas are known.

Chapter 4

Application in Near-Field UHF RFID System

4.1 Introduction

A RFID system is a spontaneous wireless data collection technology with a long history [18]. Depending upon their operating principle, RFID systems are classified into three categories: passive, semi-passive, and active. A passive RFID system is the least complex and cheapest, hence widely used for many applications. Without a power supply of a passive tag its own, the required energy to turn on the tag chip depends upon the electromagnetic field coupling from the reader. Accordingly, two different coupling techniques are further categorized: near-field coupling and far-field coupling.

Low frequency (LF, 125-134 kHz) and high frequency (HF, 13.56 MHz) RFID systems are short-range systems based on near-field coupling. On the other hand, Ultra-high frequency (UHF, 860-960 MHz) and microwave (2.4 GHz and 5.8 GHz) RFID systems are typically long-range systems based on far-field coupling. LF and HF RFID systems have been deployed in the market for many commercial applications. However, the larger size of the antennas used in the LF/HF band systems confines their further development. Thus, it is straight forward to reduce antenna size by designing the system in a higher frequency band, such as the UHF band. In addition, the near-field

UHF RFID systems have other superiorities, including higher data rate, and lower manufacturing cost, making them suitable for item-level tagging.

The near-field UHF RFID system is composed of a reader and a tag just as in the ordinary RFID systems. The simplified system architecture is depicted in Fig. 4.1. The power generated by the reader circuitry P_{reader} is transferred to the reader antenna, and then acquired by the tag antenna through near-field coupling. The power absorbed by the tag chip P_{chip} can be expressed as [19]

$$P_{chip} = P_{reader} \times \tau_{reader} \times C \times \tau_{chip} \tag{4.1}$$

where τ_{reader} and τ_{chip} are the impedance mismatch coefficients of the reader and tag between the front-end circuitry and the associated antenna, respectively. They can be expressed as

$$\begin{cases} \tau_{reader} = 1 - \left|\Gamma_t\right|^2, \ \ \Gamma_t = \dfrac{Z_T - Z_S}{Z_T + Z_S} \\ \tau_{chip} = 1 - \left|\Gamma_R\right|^2, \ \ \Gamma_R = \dfrac{Z_C - Z_R^*}{Z_C + Z_R} \end{cases} \tag{4.2}$$

Please note that since both the impedances of tag and chip are complex, we use a modified power wave reflection coefficient proposed by Kurokawa [20]. Equation (4.2) also indicates that the maximum power transfer occurs at conjugate impedance match between both components.

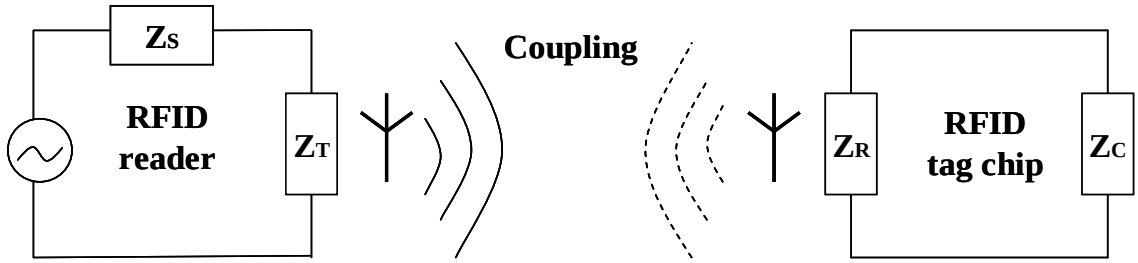

Fig. 4.1 Simplified architecture of near-field RFID systems.

C is the coupling coefficient between the reader and tag antennas. With the aid of the proposed formulation (2.7), (2,12), the coupling coefficient C can be readily calculated.

To verify the results by experiment, a near-field UHF RFID system is implemented in this chapter. In Section 4.2, we present a broadband square loop array with a back-reflector and it is used as the reader antenna. In Section 4.3, two different tag antenna designs [21], [22] are used individually in the system. We compared a series of experiments with the proposed formulation in Section 4.4. The measurement results are in good agreement with those computed by the proposed method and those simulated by HFSS as well. Furthermore, some factors are found to be crucial for improving the power coupling level in Section 4.5. For practical applications, such as Point of Sale (POS), the proposed formulation is capable of determining the near-field read range and the read reliability, which is introduced in Section 4.6. Finally, we summarized the measured results and findings in Section 4.7.

4.2 Reader Antenna

Typically, a loop antenna is favorable for a near-field reader antenna. However, the square loop with perimeter of a wavelength demonstrated in Section 3.4 is not an appropriate design due to poor concentration of power. Therefore, we develop a loop array with back-reflector to aggregate the radiated power.

The geometry of the proposed reader antenna for the near-field UHF RFID system is shown in Fig. 4.2, and the photographs are shown in Fig 4.3. Two printed square loop antennas, of which the perimeters are equal to a wavelength, are back-to-back connected by a coplanar strip (CPS) of length L_{cps}. The two arms of the CPS are connected respectively at their midpoints to the inner and outer conductors of the feeding coaxial cable. The coaxial cable is fed from the direction normal to the antenna plane. Although a balun could be added to slightly improve the radiation performance, the proposed design directly fed via a coaxial cable can still provide satisfactorily higher gain and well-shaped radiation pattern. As one may expect, the design radiates bi-directionally; however, most RFID reader antennas require unidirectional radiation pattern. To produce unidirectional radiation pattern and further increase the antenna gain, an electrically large, planar conducting sheet is utilized as a back reflector for the loop array as shown in Fig. 4.2 The spacing H between them is set to be approximately a quarter wavelength in free space.

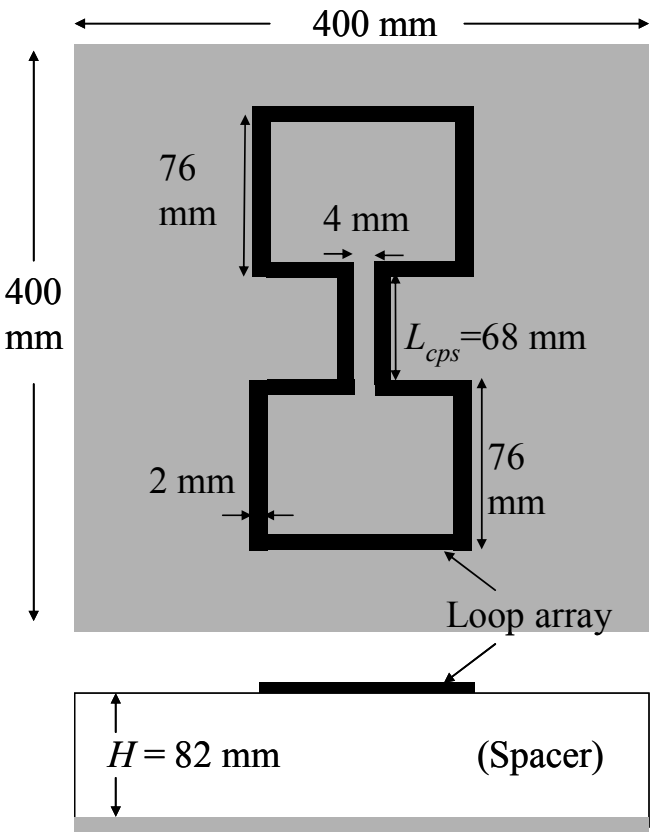

Fig. 4.2 Geometry of two-element square loop array with a back reflector.

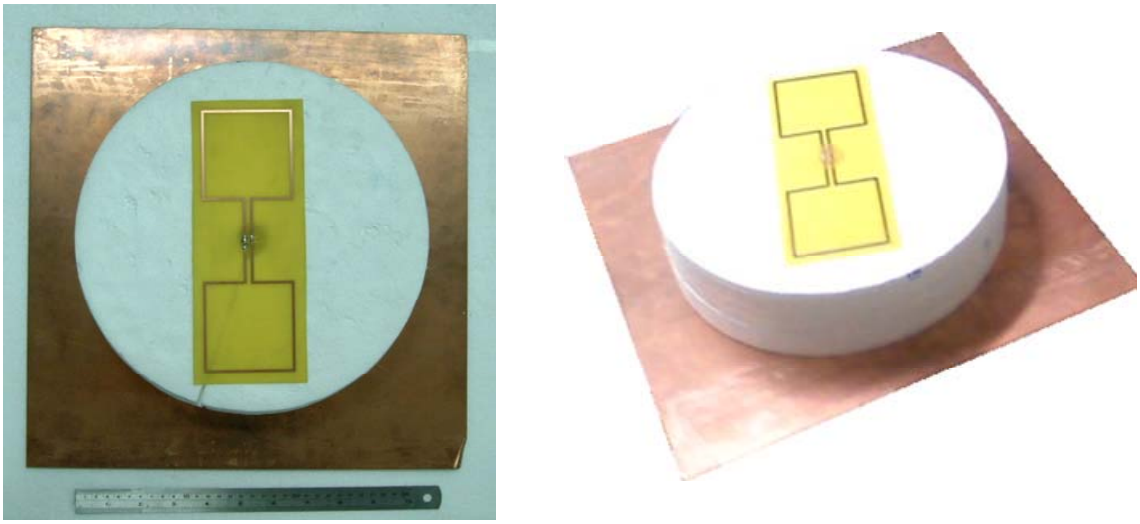

(a) (b)

Fig. 4.3 Photographs of two-element square loop array with a back reflector.

A prototype antenna designed around 915 MHz was fabricated on an FR-4 substrate with dielectric constant ε_r = 4.4 and thickness h = 0.6 mm. A copper sheet of dimensions 400×400 mm^2 is used as the back reflector and placed at a distance H = 82 mm from the loop array. Throughout the design process, simulations are carried out on HFSS. The simulated and measured input return losses of this antenna are shown and compared in Fig. 4.4. We can find that the design is well matched within a wide frequency range, and the measured 10-dB return loss bandwidth is 19.1% (848-1022 MHz). The peak gains measured at 920 MHz and 930 MHz are 10.2 and 10.1 dBi, respectively. Since the radiation pattern remains nearly the same throughout the return loss bandwidth, for simplicity, Fig. 4.5 depicts the x-z and y-z plane patterns measured at 920 MHz only.

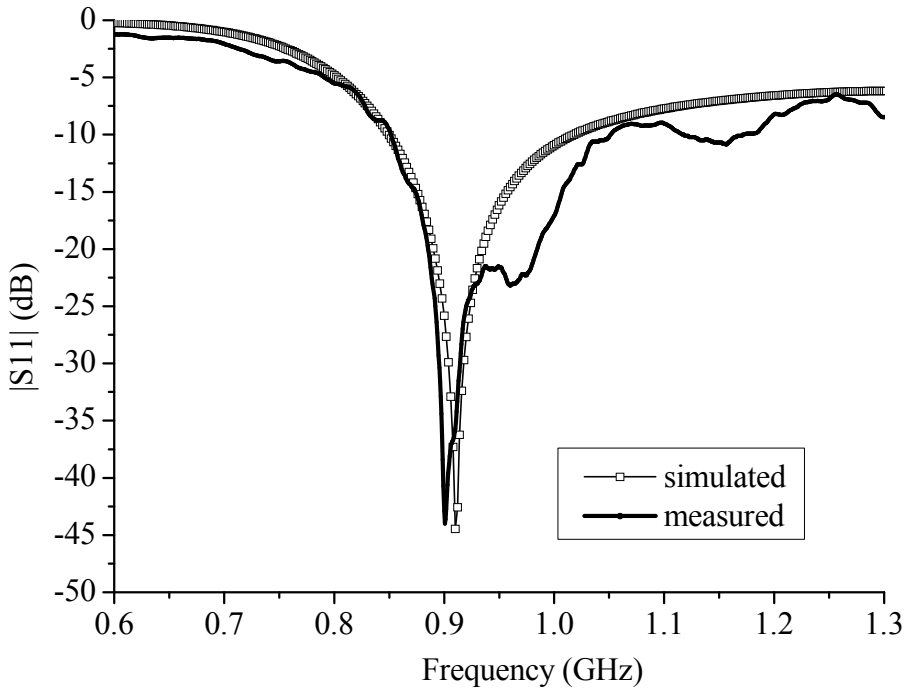

Fig. 4.4 Simulated and measured input return losses of the reader antenna.

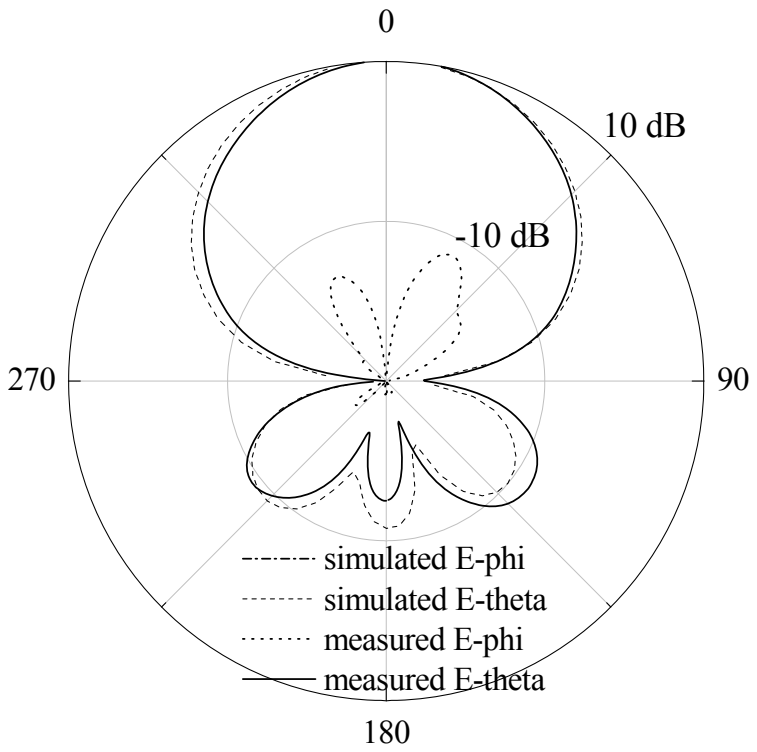

(a)

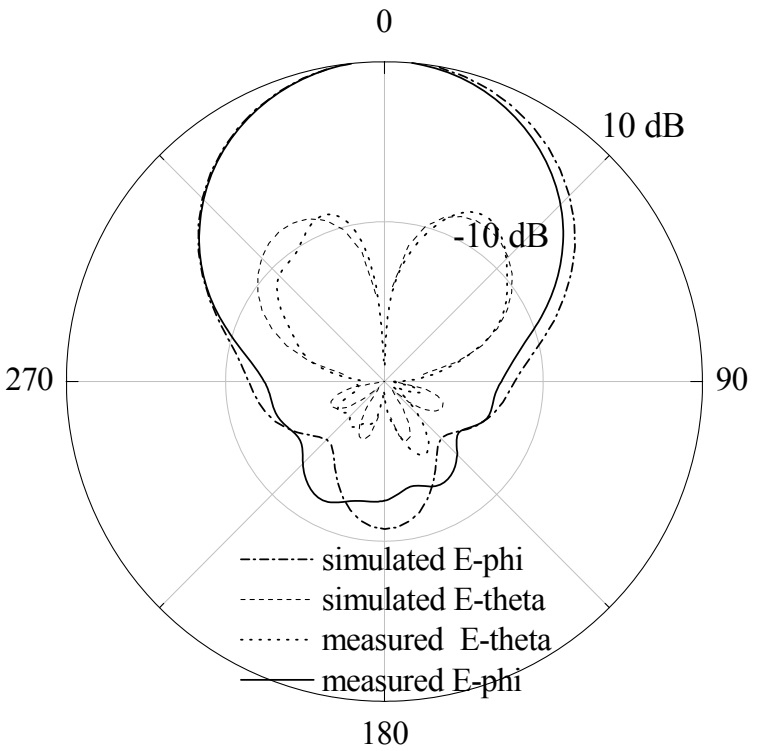

(b)

Fig. 4.5 Simulated and measured radiation patterns of the proposed reader antenna at 920MHz. (a) x-z plane and (b) y-z plane.

4.3 Tag Antennas

Passive tags utilize the coupled energy from a reader to power up the chip circuit. To have a superior power transfer between the tag antenna and the chip, the input impedance must be conjugate matched to the chip impedance, which is highly capacitive generally. The capacitive reactance of chip impedance makes the matching task become difficult between tag antenna and chip. Thus the design guidance of tag antennas is miniaturized as well as a well-coupled power. Two different tag antenna designs, referring to [21] and [22] are implemented. Each of them is used in our near-field experiment setup.

4.3.1 Folded Dipole with a Closed Loop

The first one is a folded dipole with a closed loop [21] whose main advantage is its tunable input impedance to achieve conjugate match for various commercial tag chips. A prototype antenna design at 915 MHz is depicted in Fig. 4.6, and the photograph of the antenna, of which the total antenna area is 64.4 × 27.6 mm^2, is shown in Fig. 4.7. Please note that, to facilitate measuring the coupling coefficient through the vector network analyzer (VNA), the antenna is designed for 50 Ω instead of being conjugate matched to the highly capacitive tag chips and is fed by a section of CPS connected to a balun connected to the coaxial cable. This additive balun degrades the

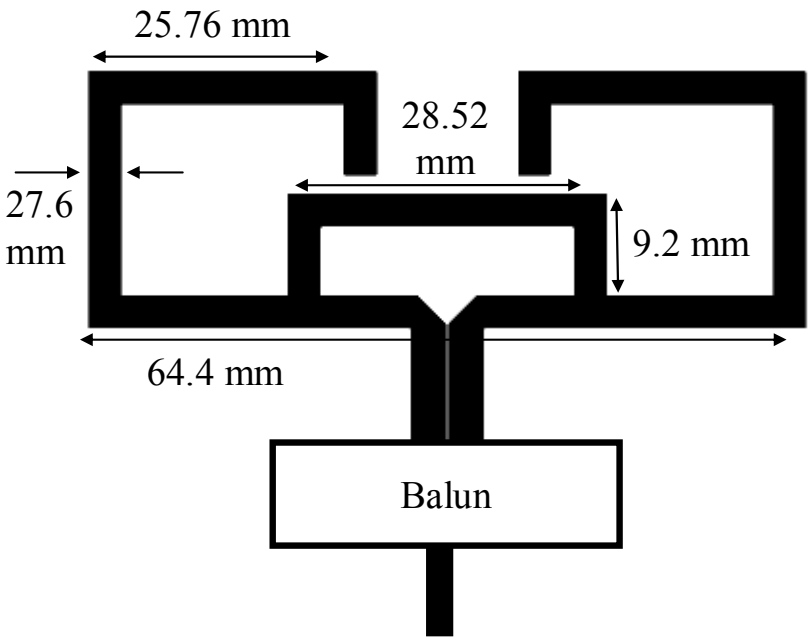

Fig. 4.6 Geometry of the folded dipole antenna.

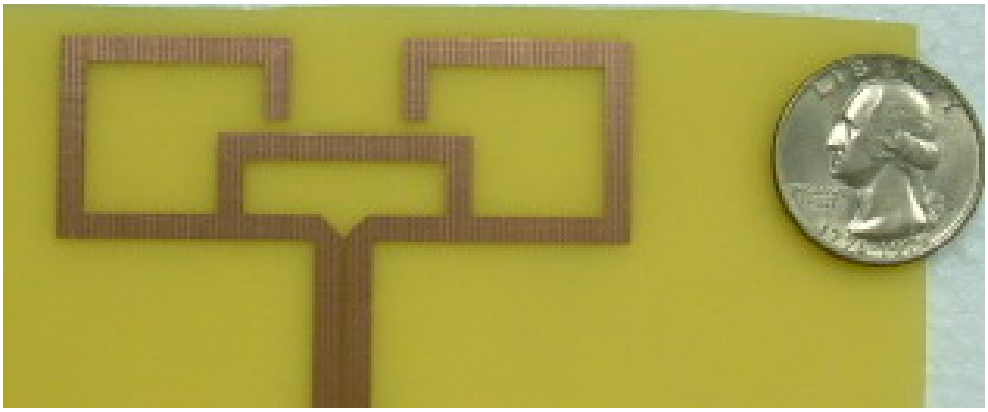

Fig. 4.7 Photograph of the folded dipole antenna.

pattern of the tag antenna inevitably, which will be stated and discussed at Section 4.3.3.

The proposed folded dipole was fabricated on the FR-4 with thickness of 0.6 mm. The simulated and measured return losses of the folded dipole with the Balun are shown and compared in Fig. 4.8, and the radiation patterns of x-z plane and y-z plane are

shown in Fig. 4.9. Due to the fabrication errors and the uncertainty of the dielectric constant of FR4, the resonant frequency of the prototype antenna slightly shifts from the design frequency of 915 MHz to 920 MHz. The peak gain measured at 920 MHz is 2.2 dBi. We can utilize this tag for near-field applications by operating at a lower output power of reader, so the tag responds only to stronger fields in the vicinity of the reader antenna.

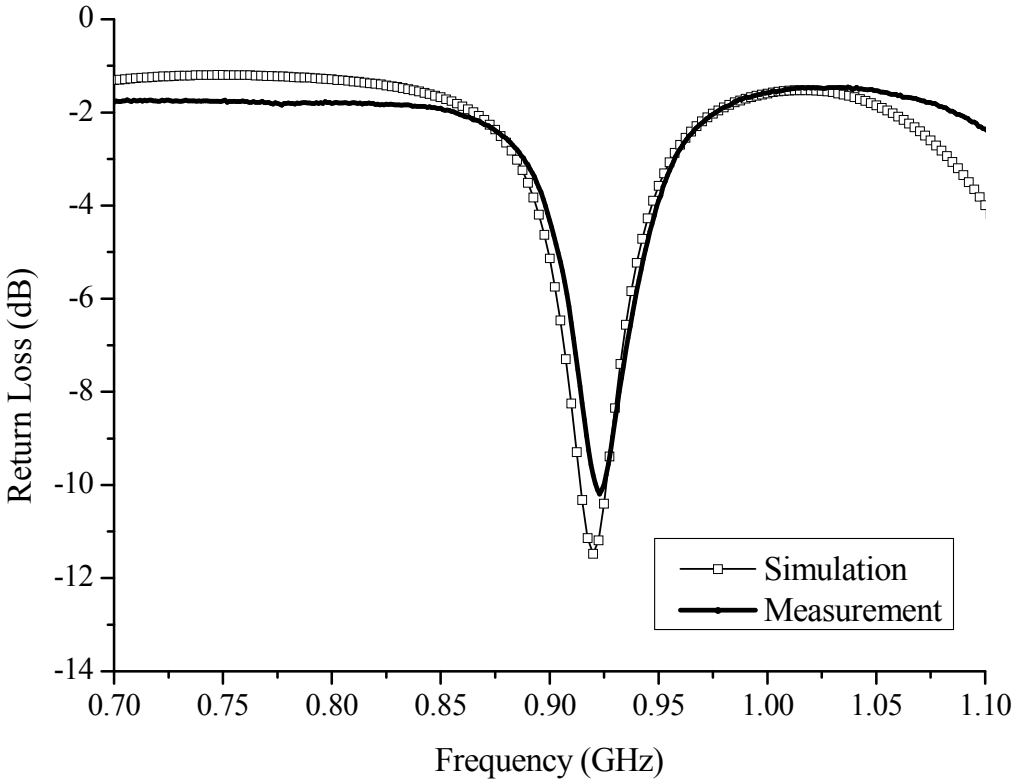

Fig. 4.8 Simulated and measured return losses of the folded dipole with the Balun

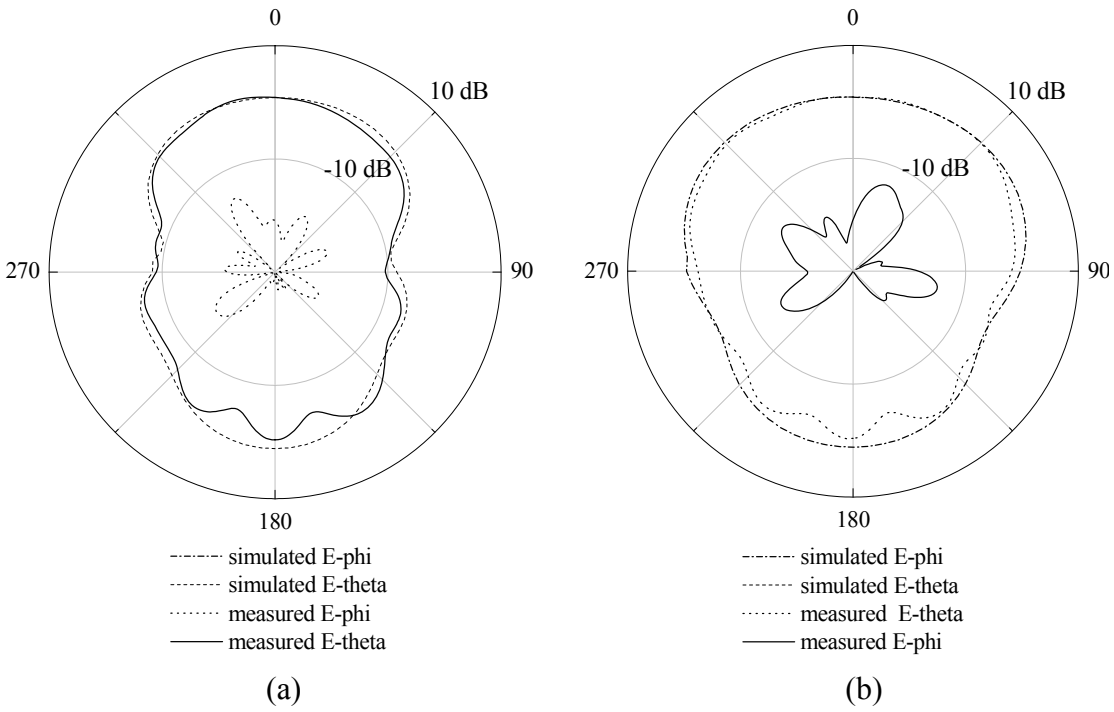

Fig. 4.9 Simulated and measured radiation patterns of the folded dipole with the Balun at 920MHz (a) x-z plane and (b) y-z plane.

4.3.2 Meander Circular Loop

The other design used is a meandered circular loop [22]. A print planar type circular loop antenna is able to reduce size by adding stubs attached to the structure. The prototype antenna designed at 915 MHz is depicted in Fig. 4.10. It is also designed for 50 Ω, and the same feeding structure is used for measurement's sake. The fabrication of the proposed meander loop was on the FR-4 with thickness of 0.6 mm. Fig. 4.11 shows the return losses obtained from simulation and measurement, and Fig. 4.12 shows the radiation patterns of the x-z plane and y-z plane. Both the return losses and radiation patterns of CPS-fed meander loop are evaluated with the Balun, and the peak gain measured at 930 MHz is 2.7 dBi.

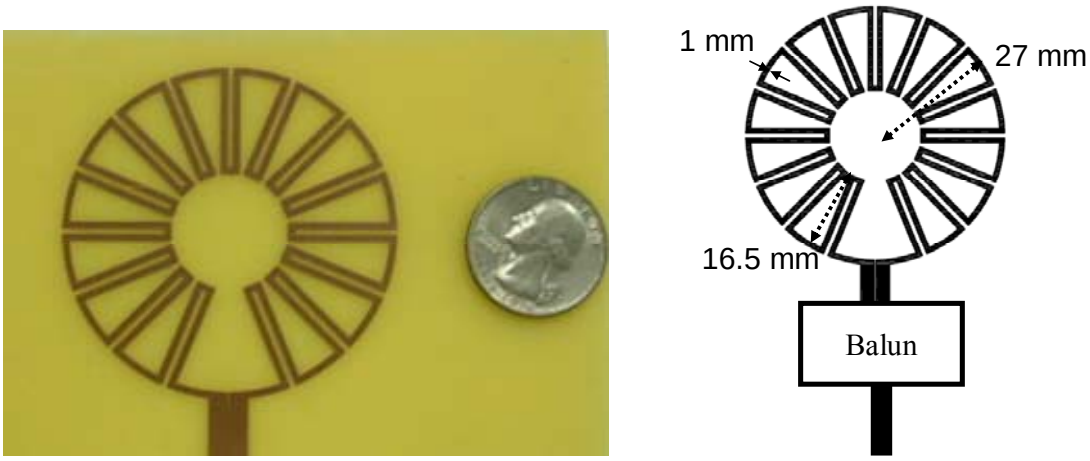

(a) (b)

Fig. 4.10 (a) Photograph of 930-MHz meander loop. (b) Geometry of meander loop fed by CPS and balun.

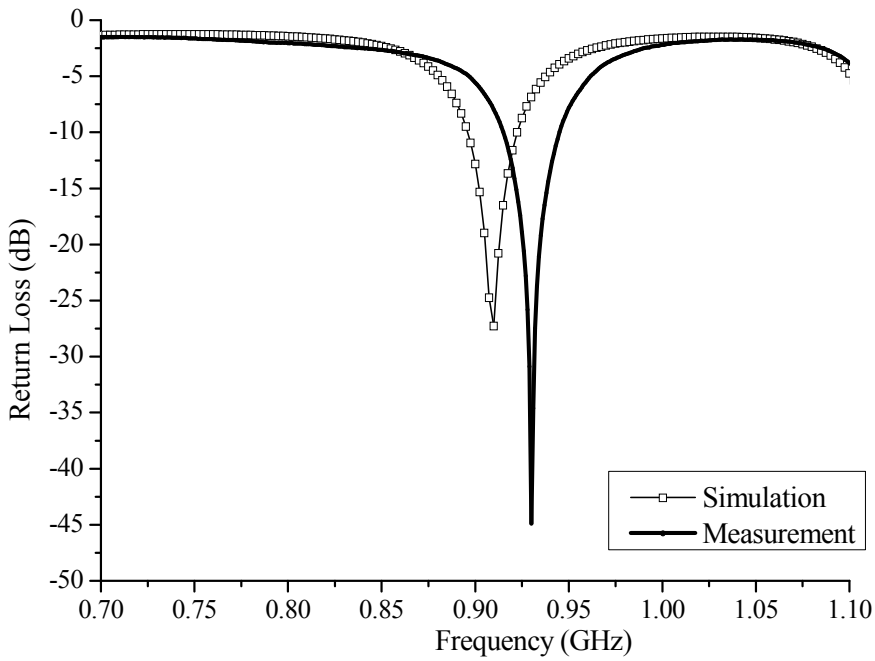

Fig. 4.11 Simulated and measured return losses of the meander loop with the Balun

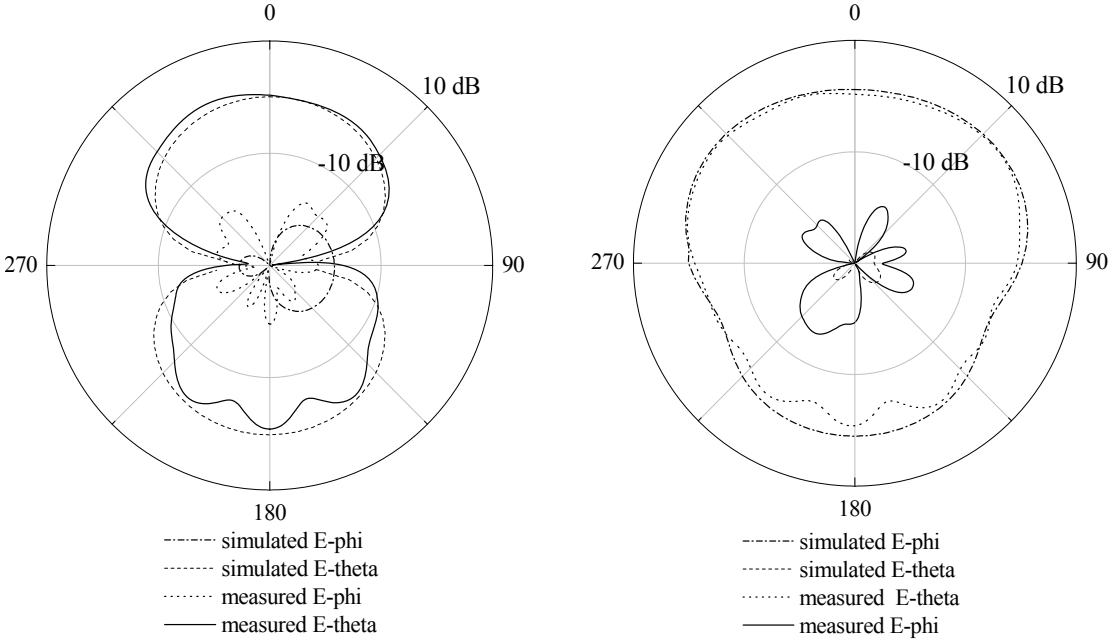

(a) (b)

Fig. 4.12 Simulated and measured radiation patterns of the meander loop with the Balun at 930MHz (a) x-z plane and (b) y-z plane.

4.3.3 Microstrip-to-CPS Transition

A coplanar stripline (CPS) is a balanced transmission line which can be used for balanced fed-in antennas such as dipoles and loops. On the other hand, a microstrip line is an unbalanced transmission line, and is one of the most widely used transmission lines in microwave circuits. In many cases, when a transition (balun) is used between the microstrip line and the CPS, the overall antenna performance is limited by the balun structure. At this section, we digress and discuss the balun used in the above-mentioned tag antennas.

The proposed balun operates from 890 MHz to 945 MHz with an insertion loss ratio (S_{21}) less than 1 dB and return loss (S_{11}) better than 10 dB for back-to-back

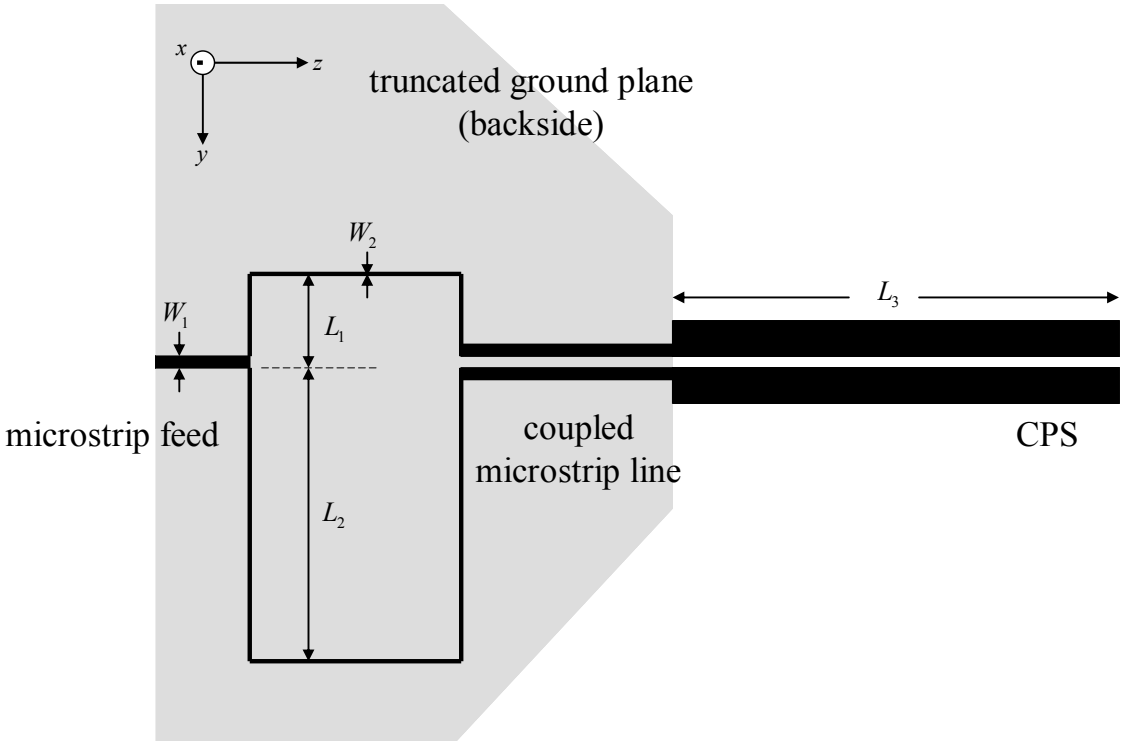

Fig. 4.13 Proposed structure of the microstrip-to-CPS transition.

transition. In spite of a narrow band, however, its bandwidth is wide enough for our application. Figure 4.13 shows the back-to-back uniplanar microstrip-to-CPS transition. It consist of a 50 Ω microstrip line (W_1 = 1.3 mm) which branched into two paths. The characteristic impedance of each microstrip branch is chosen as 100 Ω (W_2 = 0.265 mm) for easy fabrication. The differential 180° phase difference between two microstrip line branches can be accomplished by introducing a delay line where $L_2 - L_1 = \lambda_g / 4$ [23] with λ_g the guided wavelength in the microstrip. This result indicates that the dominant mode of coupled-microstrip line is odd mode, which can be subsequently utilized as a fed-in structure to balanced antenna. The gap of the CPS is 0.4 mm, strip width is 3 mm, and the CPS characteristic impedance is 50 Ω verified by HFSS.

The limitation of the proposed balun is that it degrades the radiation patterns. In Fig. 4.9 (b), the pattern in y-z plane is supposed to be omni-directional instead of reflecting fields toward the positive z-direction. A similar phenomenon can be found in Fig 4.12 (b). These inaccuracies are attributed to the truncated ground plane which reflects the power from tag antennas, hence excessive power radiates in the y direction. Two attempts have been made for eliminating such excessive power. The first one is to extend the length of CPS. In our design, L_3 is chosen as $\lambda_0/4 \approx 82\ mm$. The other manner employs a 45° tapered ground plane, as shown in Fig 4.13. The current flowing on both sides of tapered ground planes are canceled out due to their opposite phases. Further optimization of the balun and antenna design is possible depending on the requirements of particular application.

4.4 Measurement Results

The aforementioned reader and tag antennas are utilized to measure the coupling coefficient in the near-field UHF RFID system. The experiment setup is shown in Fig. 4.14. The measurements are performed in an anechoic chamber, and the associated coupling coefficients are obtained by measuring the $|S_{21}|^2$ at the antenna terminals by the HP8753D VNA depicted in Fig. 4.15. We introduce the experiments in two subsections here, that is, the coupling coefficients versus longitudinal displacements and transverse

displacements, respectively.

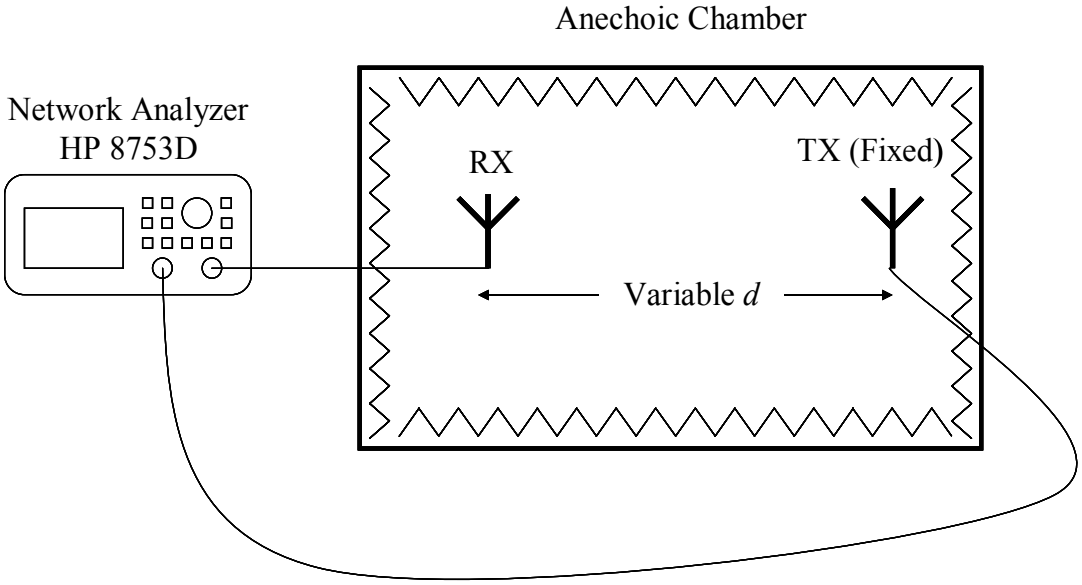

Fig. 4.14 Measurement setup for the near-field RFID system.

Fig. 4.15 Photograph of HP8753D VNA.

4.4.1 Coupling Coefficient versus Longitudinal Displacement

First of all, the coupling coefficients are measured for various antenna separations *d*, and two sets of data are acquired respectively using the two tag antennas. During the measurement, the reader antenna is fixed, while the tag antenna is moved from d = 85 mm to 400 mm with an incremental step of 5 mm. Besides, the antennas are kept polarization matched with the main beam maximum aimed at each other. A photograph of the experiment setup is shown in Fig. 4.16. Also, note that the 3D far-field patterns E_θ, E_φ needed in the formula require a finer sampling step of 1° due to the numerical integration, and therefore they are obtained by transforming the near-field measurement data.

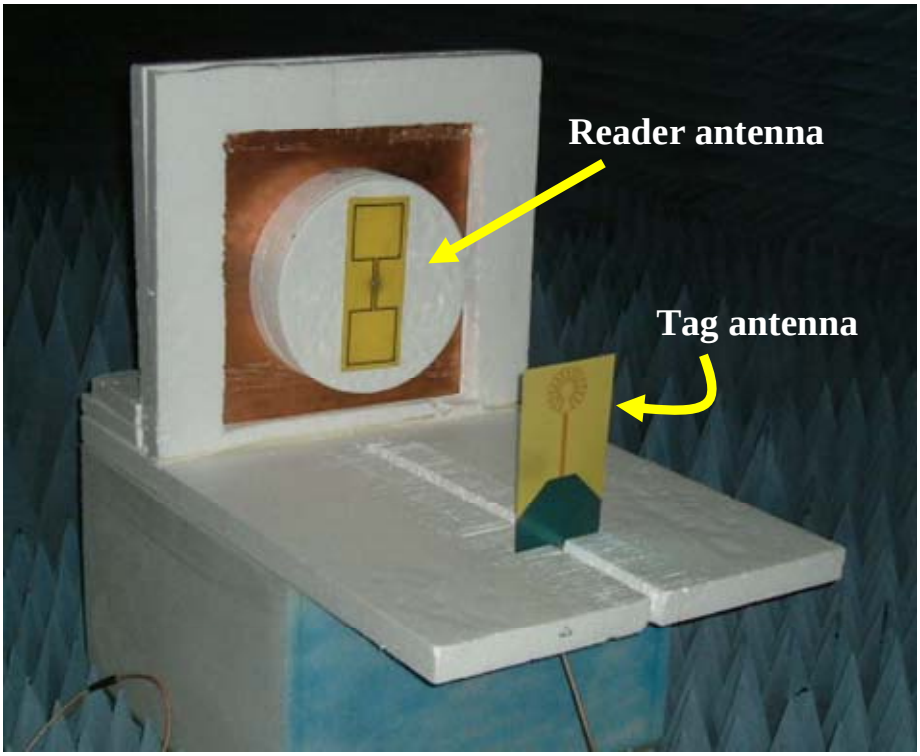

Fig. 4.16 Photograph of the measurement setup in anechoic chamber.

The coupling coefficients for the case using the folded dipole as tag antenna are measured at 920 MHz, which is the resonant frequency of the fabricated folded dipole. The measured, calculated, and full-wave simulated coupling coefficients are plotted in Fig. 4.17. Clearly, the agreement among them is quite excellent.

Then, the same measurement procedure is repeated when the folded dipole is replaced by the meandered circular loop. However, the measurement is conducted at 930MHz, namely the resonant frequency of the meandered circular loop. The results obtained are plotted in Fig. 4.18. Again, a satisfactorily good agreement can be observed among them. Figs. 4.17 and 4.18 both demonstrate the accuracy and validity of the proposed formulation.

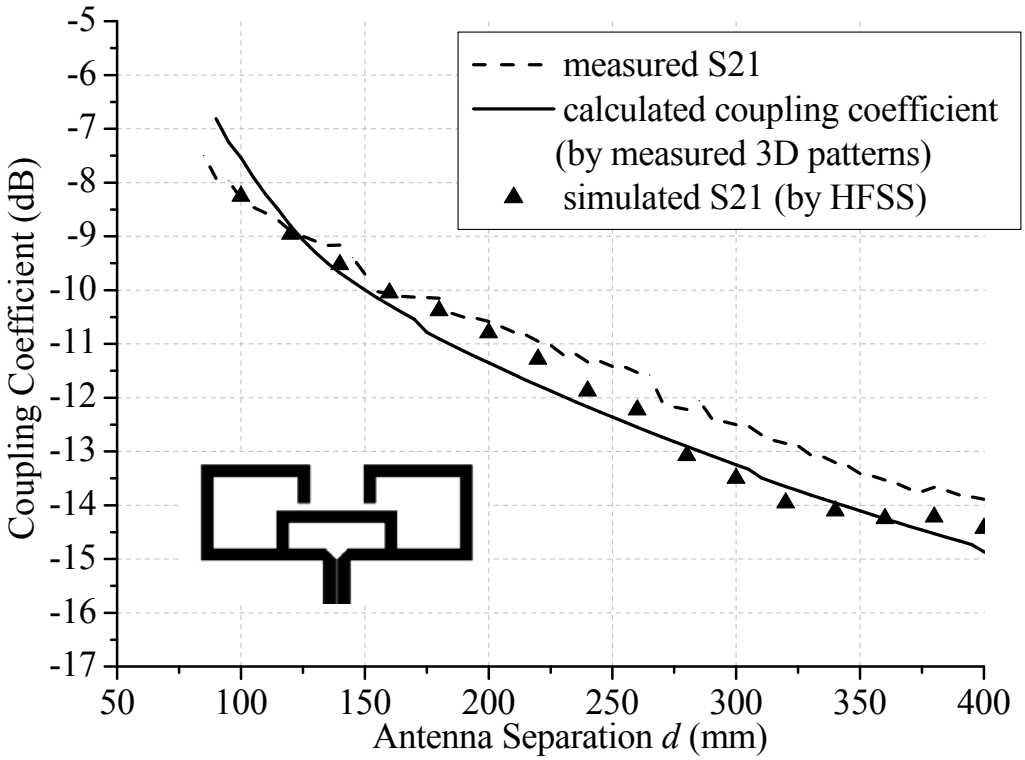

Fig. 4.17 Coupling coefficient versus antenna separation for the near-field RFID setup at 920 MHz. (Tag antenna: folded dipole)

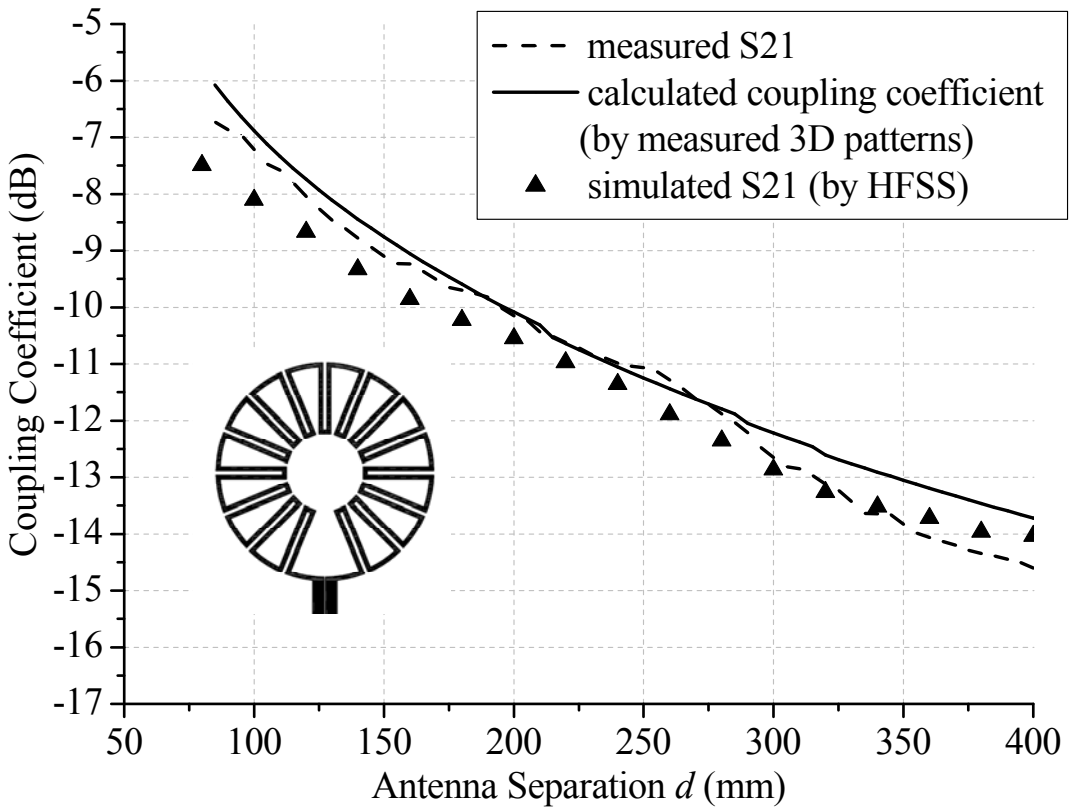

Fig. 4.18 Coupling coefficient versus antenna separation for the near-field RFID setup at 930 MHz. (Tag antenna: meandered circular loop)

4.4.2 Coupling Coefficient versus Transverse Displacement

The coupling coefficients are also obtained for the case where the tag antenna is placed at various points on a transverse plane spaced apart from the reader antenna by d. In this setup, the reader antenna is fixed, while the tag antenna "scans" on a transverse plane with a constant antenna orientation. Recalled from Section 2.3, once we have determined the transverse offsets (Δx, Δy) from the on-axis point, the transverse offsets can be converted into the relative orientation for the antennas. In addition, the 3D far-field patterns are assembled as matrices, and the field intensities are listed in θ by

row and φ by column, with sampling step of 1°. Therefore, all we need to do is to rotate the patterns with $\Delta\theta$ and $\Delta\varphi$. Please note that the antenna spacing in the formula should be *d'* instead of *d*.

Here, the folded dipole is chosen as the tag antenna, while the square loop array with a back reflector is used as the reader antenna. The measurements are made in 25-mm increments along both x- and y-axes employing a near-field planar scanner system developed by Nearfield Systems Inc, which is shown in Fig 4.19. The entire scanning area is 400×400 mm^2.

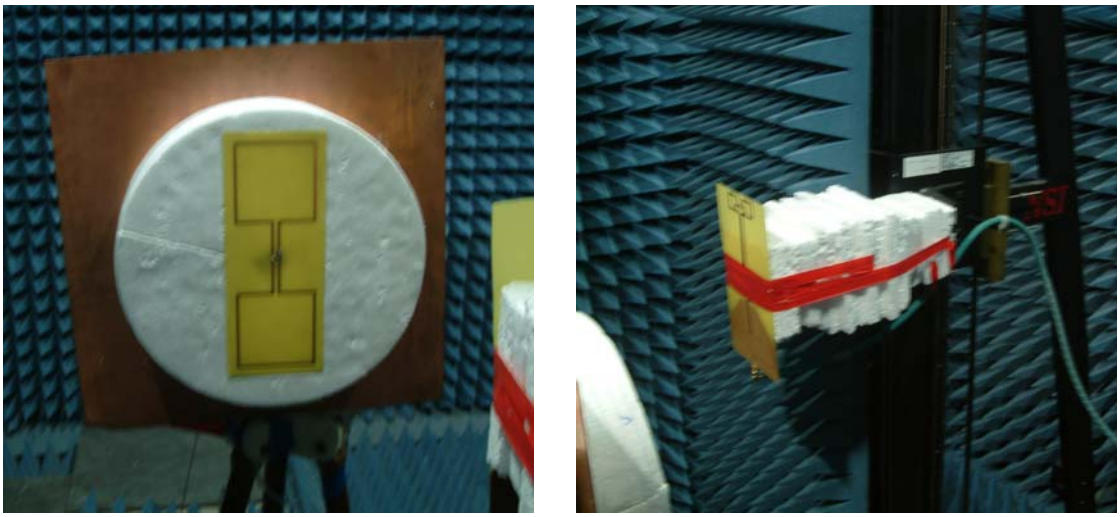

(a) (b)

Fig. 4.19 Photographs of (a) the reader antenna which is fixed at a certain position, and (b) the tag antenna which is placed on a near-field planar scanner.

The measured and calculated coupling coefficients for the transverse planes at d = 100, 200, and 300 mm are plotted in Figs. 4.20-4.22, respectively. Again, the results calculated by the formula agree very well with those measured. Note that the maximal coupling occurs at the on-axis point and the minimal coupling near the corners of the scanning area. However, near the corners, the coupling coefficient slightly increases as d is increased because the angular offset from the on-axis point becomes smaller accordingly. Therefore, as can be observed from those figures, the spatial distribution of the coupling coefficient is more uniform for a larger d. As has been discussed by the experimental verification above, we further confirm the validation of the proposed formulation.

Another contribution of the proposed formulation is that it greatly reduces the computation time. In each case, to compute the coupling coefficients by Matlab program takes about 15 minutes, while HFSS simulation would cost more than 60 hours with fine segments performing on the same computer. On the other hand, the proposed formulation also provides a scanner-based method. With the known far-field patterns of transmitting and receiving antennas, we can evaluate the near-field antenna coupling by computer in stead of measurements in an anechoic chamber.

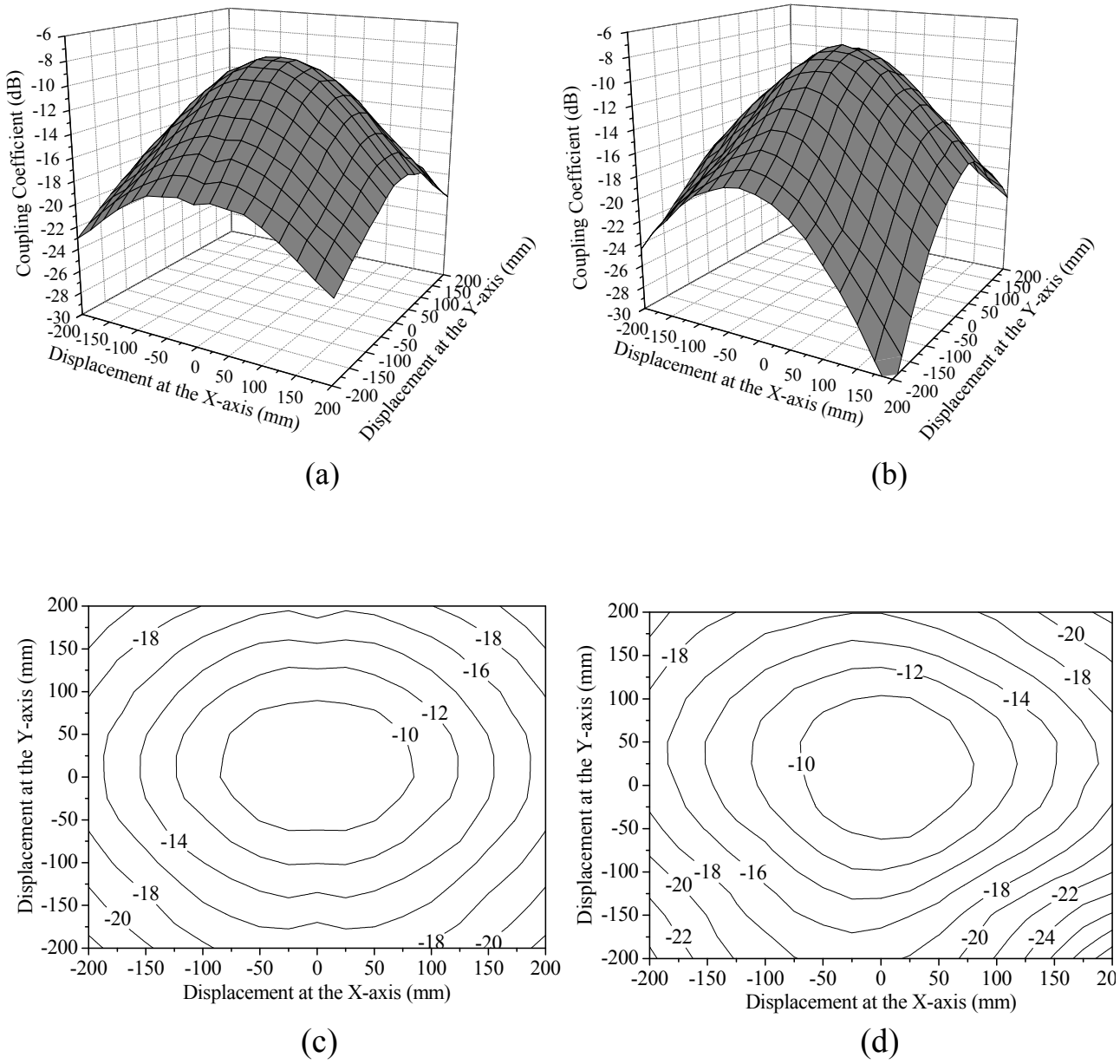

Fig. 4.20 Coupling coefficient versus transverse displacements for d = 100 mm.
(a) Calculated and (b) measured 3D surface plots, (c) calculated and (d) measured contour plots.

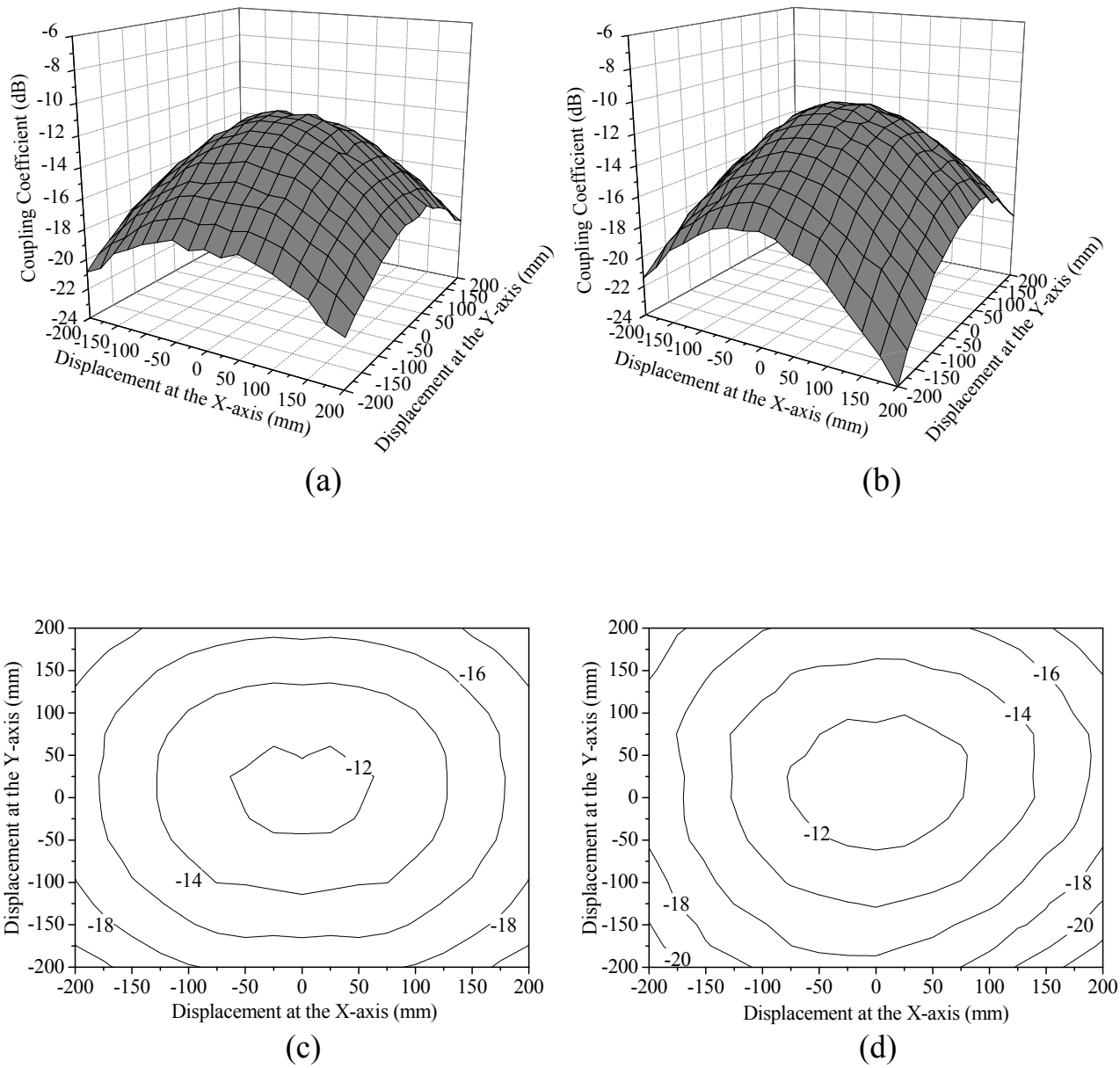

Fig. 4.21 Coupling coefficient versus transverse displacements for d = 200 mm.
(a) Calculated and (b) measured 3D surface plots, (c) calculated and (d) measured contour plots.

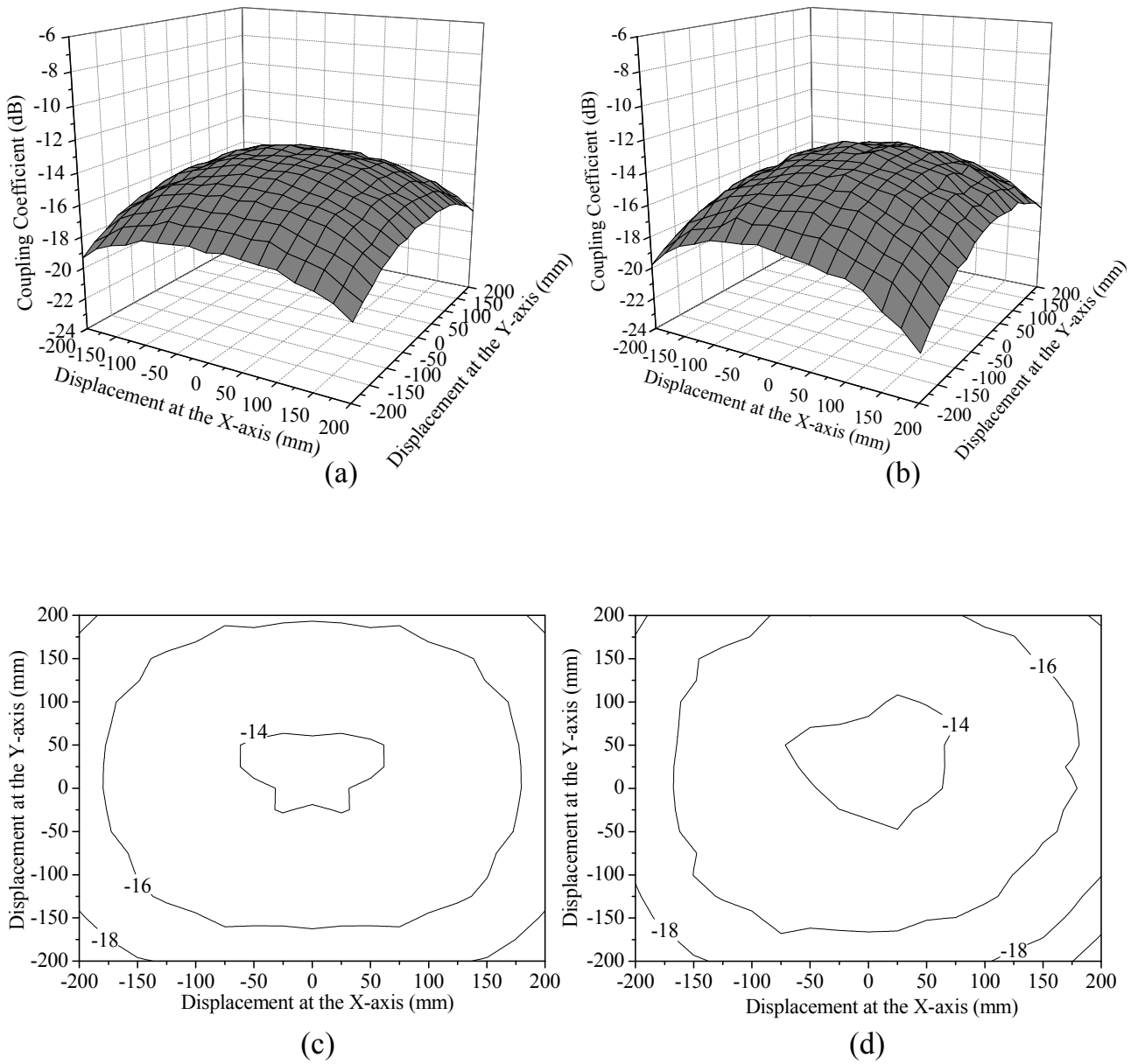

Fig. 4.22 Coupling coefficient versus transverse displacements for d = 300 mm.
(a) Calculated and (b) measured 3D surface plots, (c) calculated and (d) measured contour plots.

4.5 Enhancement of Power Coupling Level

After verifying the capability of the proposed formulation, an accompanied issue arises. Since we are aware of the coupling coefficients for certain tag-reader pairs, one fundamental question is which parameter tends to be a limiting factor for maximal power transfer. To optimize the design of reader and tag antennas, let us discuss two factors which may influence the coupling coefficient, the impedance matching of the receiving antenna and the directivity of the transmitting antenna.

4.5.1 Impedance Matching of the Receiving Antenna

Following the same procedure as Section 4.4, the coupling coefficient is investigated at frequencies other than the resonant frequency of the tag antenna here. The measurements are conducted respectively at 910, 920, 930, and 940 MHz spanning only a small fraction of the wide bandwidth of the reader antenna. For the scenario that the meander loop acts as a tag antenna, the $|S_{21}|^2$ displayed on the VNA is depicted in Fig. 4.23. One can see the maximal $|S_{21}|^2$ occurs at the resonant frequency (930 MHz) of the meander loop. Besides, the more the operating frequency deviates from resonance, the lower the $|S_{21}|^2$ would be. Replacing the folded dipole as a tag antenna, similar results are attained.

Fig. 4.23 Photograph of the curve of $|S_{21}|^2$ on the VNA.

The coupling coefficients measured and computed via the formula are compared and plotted in Figs. 4.24 and 4.25. For off-resonance operation, the associated coupling coefficient decreases mainly due to the impedance mismatch of the tag antenna.

Since large numbers of tags are being used in the supply chain and tags have a relatively short product life, the price and cost of them must be as low as possible. This requirement leads to simple antenna designs, primarily strip-line dipoles or loops. However, it is well known that strip-line antennas have relatively narrow bandwidth and short dipoles suffer from the problem of fractional bandwidth. From the above–mentioned experimental approach, we ascertain that deviations in antenna impedance from the complex conjugate of the chip impedance will significantly influence the tag performance.

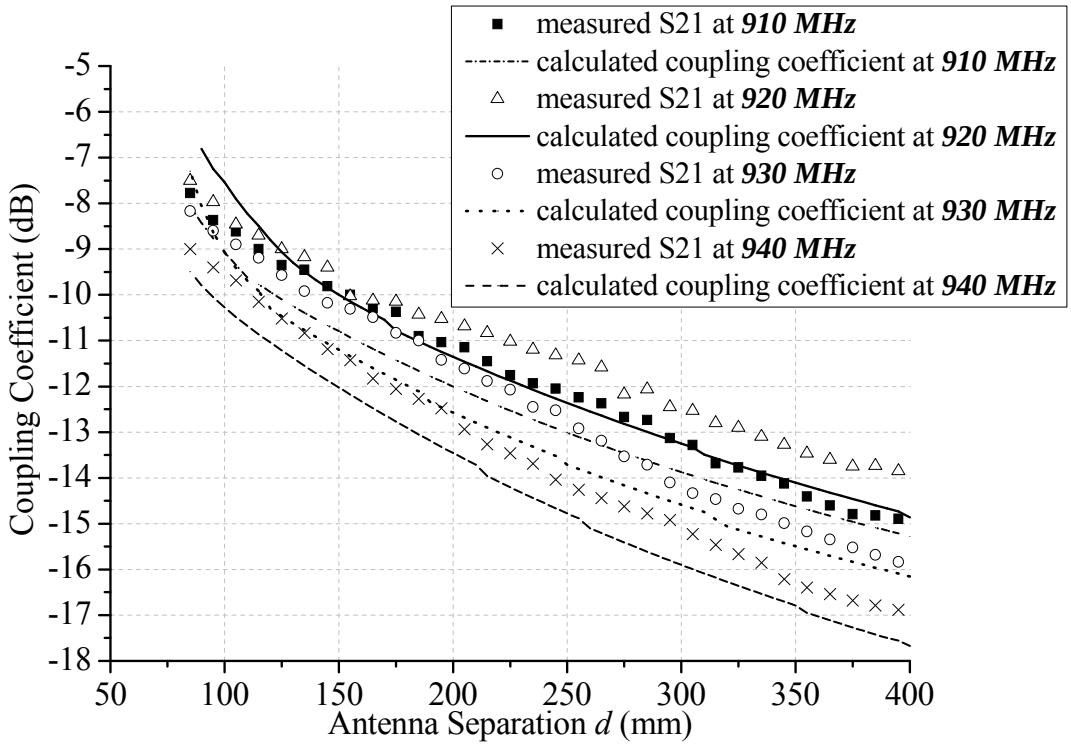

Fig. 4.24 Coupling coefficient versus antenna separation for the near-field RFID setup at 910, 920, 930, and 940 MHz. (Tag antenna: folded dipole)

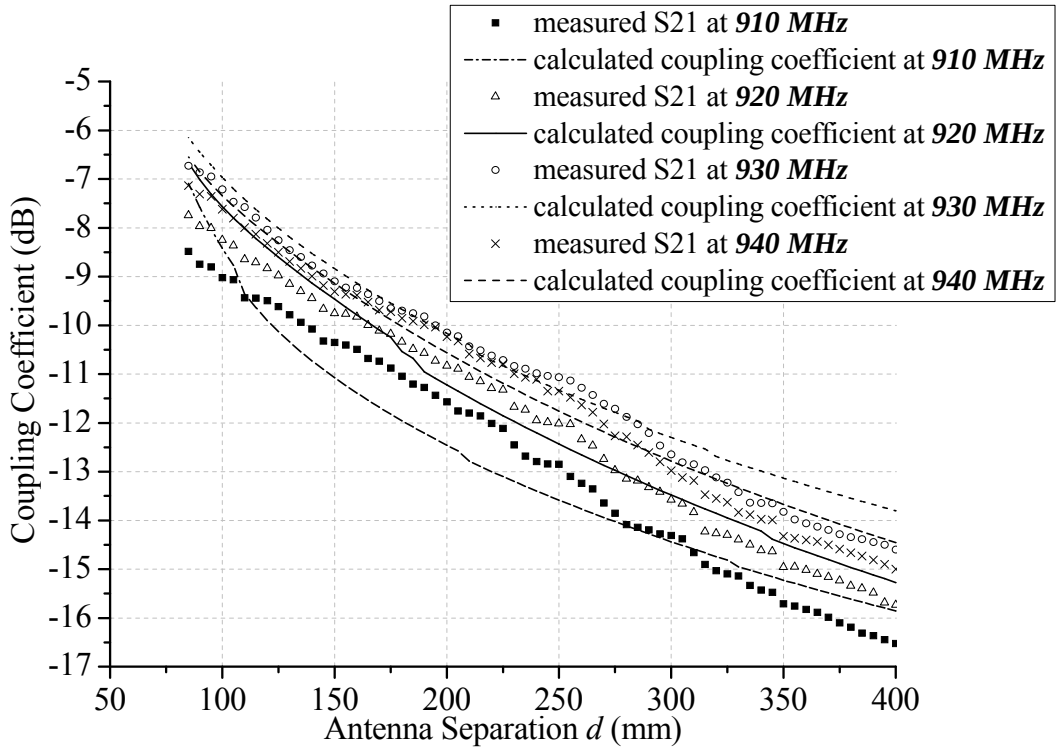

Fig. 4.25 Coupling coefficient versus antenna separation for the near-field RFID setup at 910, 920, 930, and 940 MHz. (Tag antenna: meander loop)

4.5.2 Directivity of the Transmitting Antenna

Next, additional measurements are performed by using the folded dipole as the tag antenna and replacing the proposed high-gain reader antenna by the meandered circular loop, which is designed initially as a tag antenna. Fig. 4.26 shows the measured and computed coupling coefficients along with those for the case using the proposed reader antenna. The latter exhibits a higher coupling coefficient due to the more directive far-field pattern of the reader antenna. Therefore, a reader antenna that has a higher gain is preferable in the near-field UHF RFID systems.

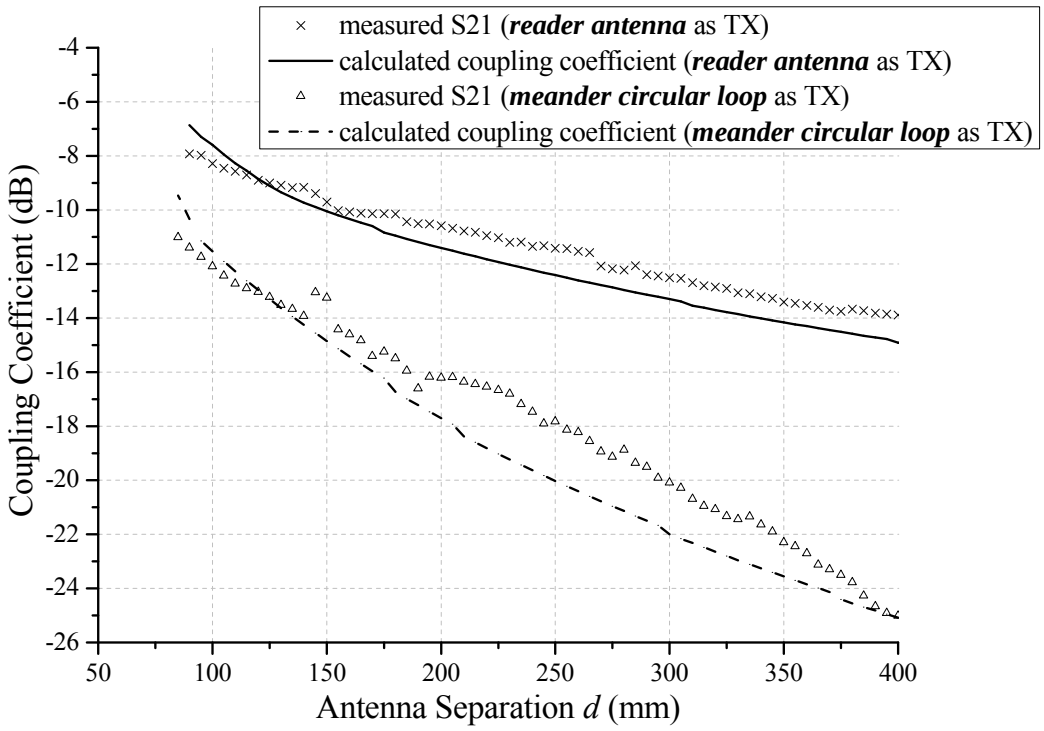

Fig. 4.26 Coupling coefficient versus antenna separation for the near-field RFID setup at 920 MHz. (Tag antenna: folded dipole. Reader antenna: meander circular loop and square loop array with back reflector)

4.6 Practical Applications of Near-Field RFID Systems

In practical applications of item-level tagging, it is required that near-field UHF RFID systems should work in a more reliable manner. In this section, we investigate two practical issues including the near-field read range and read reliability.

Typically, RFID system is strongly limited by the forward (reader-to-tag) channel power. That is, if the reader is able to provide sufficient power to the tag chip, then there will be sufficient power in the return signal to communicate with the reader. This is due to the sensitivity of readers (-90 dBm ~ -70 dBm) are higher than those of tags (-15 dBm ~ -7 dBm). Therefore, we only consider the forward link in this section. Furthermore, while we do not directly measure chip information, the consideration here is focused on the interaction between the reader and tag antennas, and we use the relation of proposed formulation (4.3) between transmitting power, receiving power, and distance.

4.6.1 Near-Field Read Range

Read range is an important characteristic of the RFID tag, even in a near-field system. It is the maximum distance which the tag can be detected. One limitation for the read range is the maximum distance which tag just receives enough power to turn on the chip circuitry, while the other limitation is the maximum distance which the reader is

able to detect the backward signal. As mentioned previously, the read range is chosen as the first one since it is normally shorter.

In near-field (UHF) RFID systems, it is desired that the tags can only be detected within a specified read range and are imperceptible beyond that. With the aid of the proposed formula, it is straightforward to determine the read range for near-field RFID systems. First, rewrite (4.1) into (4.3):

$$-C_{(dB)} = P_{reader(dB)} - P_{th(dB)} + \tau_{reader(dB)} + \tau_{chip(dB)} \tag{4.3}$$

where P_{th} is the chip sensitivity, representing the minimum threshold power necessary to power up the tag chip provided by the chip vendors.

For simplicity, it is assumed that the reader circuitry (tag chip) and the antenna are perfectly matched such that $\tau_{reader(dB)} = 0$ ($\tau_{chip(dB)} = 0$). Given the output power of the reader circuitry P_{reader} and the P_{th} of the tag chip, one can find the corresponding read range from the curve of coupling coefficient C calculated by the proposed formula regarding the coupling coefficient as a function of antenna separation for the particular reader and tag antennas used. For example, consider one of the above scenarios where the folded dipole is the tag antenna and the square loop array with a back reflector is the reader antenna. For a given $P_{th(dB)} = -3$ dBm and $P_{reader} = 10$ dBm, one can read from Fig. 4.17 that the corresponding read range for coupling coefficient $C = -13$ dB is equal to 280 mm. This information further means that the output power exceeding 10 dBm

may enable the reader to detect the tags outside the read range in addition to those within.

4.6.2 Read Reliability

We define the read reliability as the probability that a reader successfully detects and identifies a tag when a tag is in the read range of reader antenna [24]. Here, we establish a Monte Carlo simulation for determining the read reliability in free-space environment. Recalled from (4.3), typically the output power of a near-field reader is arranged from 10 dBm to 30 dBm, and the chip sensitivity varies from -15 dBm to -7 dBm. We define the threshold of the coupling loss $-C_{th(dB)}$ as the permissible maximal coupling loss under the given P_{reader} and P_{th}. For example, under the specification of P_{reader} = 10 dBm and P_{th} = -10 dBm, $-C_{th}$ = 20 dB is achieved. This definition further means that a tag antenna with $-C_{tag(dB)} > -C_{th(dB)}$ will be unreadable since the power loss in free space is too large and incapable to turn on the chip circuitry.

In the POS of a supermarket, tags are attached to objects which are packed in a basket, pass through the convey belt, and a reader under the convey belt reads the tags and processes tag information. For the operation below, the meander circular loop is chosen as the tag antenna, while the square loop array with a back reflector is used as the reader antenna and be operated at 930 MHz. We assume there is only one tag

attached to the object, and the scattering of the object is negligible. We first model the distribution of the tag position in the basket. The dimensions of the basket are 40×40×30 cm^3 as shown in Fig. 4.27 and the basket is 10 cm above the reader antenna. Although in real situations, objects would be packed onto the bottom prior to the top in the basket, for measurement's convenience, we model the distribution of the tag position as a random variable. Next, the orientation of the tag is also simulated randomly.

After those setups are accomplished, we sample 10000 data of coupling coefficients calculated from the proposed formulation (Matlab program), and they are compared with two thresholds of the coupling loss, $-C_{th}$ = 20 dB and 30 dB. On the other hand, we have conducted an experiment by collecting 500 data of $|S_{21}|^2$ identical to the simulation setup. The simulated and measured read reliability is shown as the cumulative density function (CDF) in Fig. 4.28. Also, the statistics of the results are listed in Table 4.1.

Table 4.1 Comparison between the simulation and measurement

Classification	**Read reliability**		**Coupling Coefficient (dB)**	
	$-C_{th}$ = 20 dB	**$-C_{th}$ = 30 dB**	**Mean**	**Standard derivation**
Simulation	63.2 %	96 %	-18.01	6.493
Measurement	57 %	93 %	-20.09	6.24

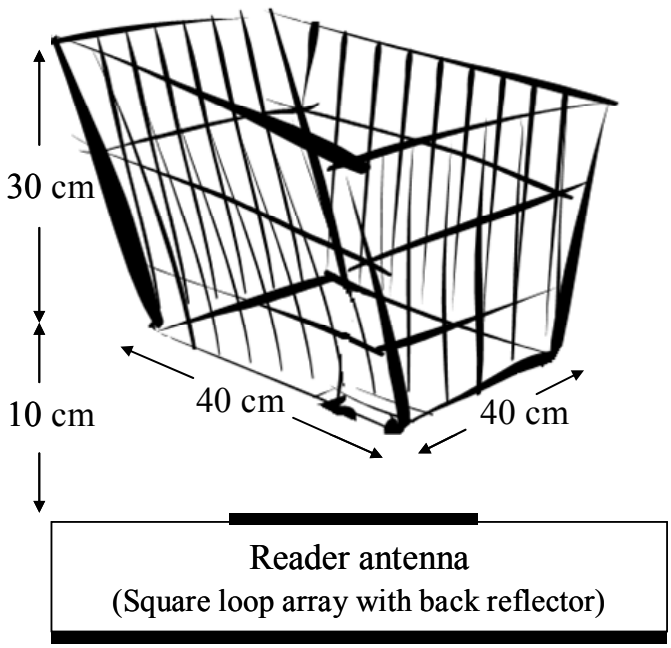

Fig. 4.27 Geometry of the basket which is 10 cm above the reader antenna.

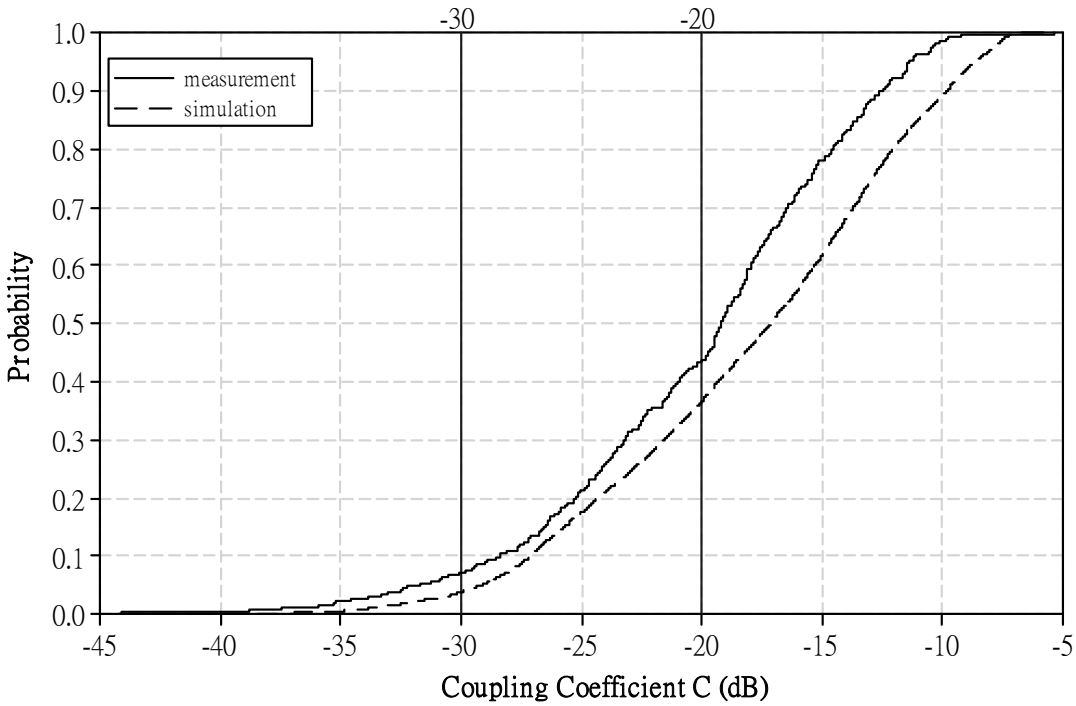

Fig. 4.28 Comparison of simulated and measured CDF of read reliabilities at 930 MHz. (Tag antenna: meander circular loop. Reader antenna: square loop array with back reflector)

4.7 Summary

We have implemented a near-field UHF RFID system, and evaluated the antenna coupling by both the analytic and experimental approaches. Our measurements reveal the fact that power coupling level depends on various kinds of factor, such as the impedance matching of a tag antenna, and the directivity of a reader antenna. In addition, we have evaluated the free-space read range and read reliability. From the practical application discussed in this chapter, the proposed formulation provides important guidelines with simplicity.

Chapter 5

Conclusion

5.1 Summary of This Thesis

Basically, this thesis focuses on the power transfer relation in near-field communication system. The kernel of the formulas (2.7), (2,12) applies to any two arbitrarily oriented and separated antennas in free space, and all the parameters we need are the relative orientation and the 3D vector far-field pattern of each antenna at a single frequency. Our major contribution is to develop a series of experiments to verify the proposed equation which can be regarded as a near-field counterpart of the Friis transmission equation. Additionally, we have proposed methods to determine the read range and the read reliability in near-field RFID systems. In this chapter, we briefly summarize our works and some important results.

In **Chapter 2**, we specify the boundary between near and far field and develop the method to simplify the proposed equation to calculate the coupling coefficient. The coupling coefficient is given by a spherical wave representation and it is also a function of the antenna separation within three-dimensional space. Although the proposed equation (2.7) is expressed by an infinite series, our method indicates that the series converges within less than ten terms.

In **Chapter 3**, the proposed formula is verified by considering three typical scenarios, and the associated results have been shown to agree well with those simulated.

In **Chapter 4**, an experiment setup for a near-field UHF RFID system is designed and implemented. The coupling coefficients obtained via the formula, measurement, and the HFSS simulation are all in good agreement. Meanwhile, some factors crucial to the coupling coefficient are identified, including the impedance matching of the receiving antenna, directivities and relative orientation of the transmitting and receiving antennas, etc. Furthermore, with the aid of the proposed formulation we can evaluate the read range and the read reliability. It is believed that the proposed formula may be useful for the design and optimization of near-field communication systems.

5.2 Future Works

As the study and discussions throughout this thesis, the near-field antenna coupling is considered by single transmitting and receiving antenna in free space, neglecting the scattering field of obstacles in environment. However, in practical RFID application, there are often multiple tags placed in the read range, and RF signal of different tags may interfere among one another. To further investigate RFID performance for practical cases and item-level tagging, it is suggested that combining

the proposed formulation with environmental factors. For example, the direction of scattering field can be constructed by a statistical model. Other possible solution is to measure the pattern of tag antenna along with the object, and substituting it into (2.12) and (2.7).

Another issue is whether UHF near-field antennas work reliably in the presence of metal and water. UHF near-field technology has been promoted by industry as a solution to the “metal and water problem” [25], however, some publications show that commercial near-field tags can not solve the “metal and water problem”. In contrary, it may degrade the performance worse than far-field tags [26]. Therefore, it is a worthy research to derive a rigorous analysis of the UHF near-field antenna especially in developing the proposed formulation that includes the presence of metal or water near the tag antenna. By means of proper physics understanding, some approaches may be conducted to lead to a more general model.

Appendix

In this thesis, we focus on the power transfer relation in near-field communication. The kernel of the proposed formulation is evaluating the coupling quotient as a solution of the scalar Helmholtz equation, so it can be expanded in a series of spherical wave functions by giving the spherical wave coefficients B_{nm} as unknown. Next, we use the orthogonality relationships of tesseral harmonics to evaluate the B_{nm}. In this appendix, the coupling quotient in terms of normalized far-field patterns is introduced detailedly, which is done by Yaghjian [15]. In the second place, we derive the series expansion of spherical wave functions and spherical wave coefficients. The derivations below are also mentioned in [16], and we emphasize the associated sections in this thesis.

A.1 Coupling Quotient in Terms of Far-Field Patterns

The theory of the coupling quotient begins with the Kerns "transmission integral" (To the authors' best effort, the original publication of Kerns can not be founded in June 2009), which express the coupling quotient in terms of the transmitting and receiving plane-wave characteristics of each antenna:

$$\frac{b_R}{a_T} = \frac{1}{1-\Gamma_R\Gamma_L}\int_{-\infty}^{\infty}\int_{-\infty}^{\infty} s'_{02}(\mathbf{k})\cdot s_{10}(\mathbf{k})e^{i\mathbf{k}\cdot\mathbf{r}}dk_x dk_y \tag{A.1}$$

where $s_{10}(\mathbf{k})$ and $s'_{02}(\mathbf{k})$ are the vector transmitting and receiving characteristics defined

with respect to plane waves traveling in the **k** direction but with phase referenced to the phase center of each antenna. Other definitions of symbols are identical to those in Chapter 2.3.1. Equation (A.1) is an exact solution from Maxwell's equations, and the assumptions are neglecting multiple reflections between two antennas. However, (A.1) cannot be used to compute b_R/a_T unless the characteristic s_{10} and s'_{02} are transformed to commonly measured parameters of the antennas.

We first transform the receiving functions s'_{02} into its transmitting function s'_{20} by reciprocity theorem:

$$\frac{s'_{02}(\mathbf{k})}{Z_{RFeed}} = \frac{k_z}{k\eta} s'_{20}(-\mathbf{k}) \tag{A.2}$$

Again, all parameters have been defined in Chapter 2.3.1. Substituting s'_{02} from (A.2) into (A.1) gives

$$\frac{b_R}{a_T} = \frac{Z_{RFeed}}{k\eta(1-\Gamma_R\Gamma_L)} \iint_{K<k} k_z s'_{20}(-\mathbf{k}) \cdot s_{10}(\mathbf{k}) e^{i\mathbf{k}\cdot\mathbf{r}} dk_x dk_y \tag{A.3}$$

Note that the integral interval in (A.3) has been made to $K < k$ by leaving only the radiating part of the spectrum. The radiating characteristics s_{10} and s'_{20} for $K < k$ are related to the normalized complex electric far-field patterns by

$$\begin{cases} s_{10}(\mathbf{k}) = \dfrac{i}{k_z} f_T(\mathbf{k}) \\ s'_{20}(-\mathbf{k}) = \dfrac{i}{k_z} f_R(-\mathbf{k}) \end{cases} \tag{A.4}$$

Substituting (A.4) into (A.3) produces the coupling quotient for two antennas as a

double integral over the inner product of the complex electric far-field patterns of the antennas:

$$\frac{b_R}{a_T} = -\frac{C_R}{k} \iint_{K<k} \frac{f_R(-\mathbf{k}) \cdot f_T(\mathbf{k})}{k_z} e^{i\mathbf{k}\cdot\mathbf{r}} dk_x dk_y \tag{A.5}$$

where C_R is consolidated notation for the mismatch factor

$$C_R = \frac{Z_{RFeed}}{\eta(1-\Gamma_R\Gamma_L)} \tag{A.6}$$

The coupling quotient b_R/a_T expressed in (A.5) and (A.6) are identical to (2.2) and (2.3).

A.2 Series Expansion of Spherical Wave Functions

We first consider the scalar Helmholtz equation $(\nabla^2 + k^2)\psi = 0$ in spherical coordinates:

$$\frac{1}{r^2}\frac{\partial}{\partial r}\left(r^2 \frac{\partial \psi}{\partial r}\right) + \frac{1}{r^2 \sin\theta}\frac{\partial}{\partial \theta}\left(\sin\theta \frac{\partial \psi}{\partial \theta}\right) + \frac{1}{r^2 \sin^2\theta}\frac{\partial^2 \psi}{\partial \phi^2} + k^2\psi = 0 \tag{A.7}$$

To solve the solution ψ, we use the method of separation of variables and let

$$\psi = R(r)H(\theta)\Phi(\phi) \tag{A.8}$$

Substituting (A.8) into (A.7), dividing by ψ, and multiplying by $r^2 \sin^2\theta$, we attain

$$\frac{\sin^2\theta}{R}\frac{d}{dr}\left(r^2 \frac{dR}{dr}\right) + \frac{\sin\theta}{H}\frac{d}{d\theta}\left(\sin\theta \frac{dH}{d\theta}\right) + \frac{1}{\Phi}\frac{d^2\Phi}{d\phi^2} + k^2 r^2 \sin^2\theta = 0 \tag{A.9}$$

For proper choosing constants m and n, we can completely separate (A.9) into three independent equations:

$$\frac{d}{dr}\left(r^2\frac{dR}{dr}\right)+\left[(kr)^2-n(n+1)\right]R=0$$
$$\frac{1}{\sin\theta}\frac{d}{d\theta}(\sin\theta\frac{dH}{d\theta})+\left[n(n+1)-\frac{m^2}{\sin^2\theta}\right]H=0 \tag{A.10}$$
$$\frac{d^2\Phi}{d\phi^2}+m^2\Phi=0$$

Note that the constant m and n are independent.

The R equation is related to Bessel's equation. Its solution is a combination of the spherical Bessel function of the first and second kinds, denoted by $j_n(kr)$ and $y_n(kr)$, respectively. Typically these two functions represent standing waves. On the other hand, to express a plane-wave characteristic, it is convenient to define the spherical Hankel function of the first and second kinds as

$$\begin{aligned} h_n^{(1)}(kr)&=j_n(kr)+iy_n(kr)\\ h_n^{(2)}(kr)&=j_n(kr)-iy_n(kr)\end{aligned} \tag{A.11}$$

$h_n^{(1)}(kr)$ represents an inward-traveling wave, while $h_n^{(2)}(kr)$ represents an outward-traveling wave. To expand the near-field coupling quotient, empirically we choose $h_n^{(1)}(kr)$ as the basis in our formulation.

The H equation is related to Legendre's equation, and their solutions are called associated Legendre functions. We express them as $P_n^m(\cos\theta)$ and $Q_n^m(\cos\theta)$, with associated Legendre polynomials of the first and second kind, respectively. A study of

associated Legendre polynomials shows that all functions have singularities at $\theta = 0$ or $\theta = \pi$ except $P_n^m(\cos\theta)$ with n as an integer. Since ψ should be finite in the range 0 to π on θ, then n must be an integral and we choose $P_n^m(\cos\theta)$ as our basis.

The Φ equation is a so-called harmonics equation, and the solution of the harmonic equation are called harmonic functions and denoted by $h(m\phi)$. Commonly used harmonic functions in spherical coordinates are

$$\sin m\phi,\ \cos m\phi,\ e^{im\phi},\ e^{-im\phi} \tag{A.12}$$

Since a single-valued ψ in the range 0 to 2π on ϕ is desired in our formulation, we choose $h(m\phi)$ to be a linear combination of $e^{im\phi}$ and $e^{-im\phi}$.

Summarize the above discussions, we can form product solutions ψ to the scalar Helmholtz equation as

$$\psi_{m,n} = h_n^{(1)}(kr) P_n^m(\cos\theta) e^{im\varphi} \tag{A.13}$$

are the desired elementary functions for the coupling quotient with m and n integrals. To construct more general solutions, we construct linear combinations of the elementary function as

$$\begin{aligned} \psi &= \sum_{n=0}^{\infty} \sum_{m=-n}^{n} B_{nm} \psi_{m,n} \\ &= \sum_{n=0}^{\infty} \sum_{m=-n}^{n} B_{nm} h_n^{(1)}(kr) P_n^m(\cos\theta) e^{im\varphi} \end{aligned} \tag{A.14}$$

where B_{nm} are the unknown spherical wave coefficients. Here we sum up all possible values of m and n, and the remaining work is to evaluate the unknown spherical wave

coefficients B_{nm}.

A.3 Orthogonality Relationship of Tesseral Harmonics

The orthogonality relationships state that an arbitrary function $f(\theta,\phi)$ defined over the surface of a sphere can be expanded in a series of tesseral harmonics. Here the tesseral harmonics of nth degree and mth order are defined as the functions $T_{mn}^{e}(\theta,\phi)=P_n^m(\cos\theta)\cos m\phi$ and $T_{mn}^{o}(\theta,\phi)=P_n^m(\cos\theta)\sin m\phi$. In other words, $f(\theta,\phi)$ can be represented as

$$f(\theta,\phi)=\sum_{n=0}^{\infty}\left[a_{0n}P_n(\cos\theta)+\sum_{m=1}^{n}\left(a_{mn}\cos m\phi+b_{mn}\sin m\phi\right)P_n^m(\cos\theta)\right] \quad \text{(A.15)}$$

whose coefficients are determined by

$$\begin{aligned}
a_{0n}&=\frac{2n+1}{4\pi}\int_0^{2\pi}\int_0^{\pi}f(\theta,\phi)P_n(\theta,\phi)d\theta\, d\phi\\
a_{mn}&=\frac{2n+1}{2\pi}\frac{(n-m)!}{(n+m)!}\int_0^{2\pi}\int_0^{\pi}f(\theta,\phi)P_n^m(\cos\theta)\ \cos m\phi\ \sin\theta d\theta\, d\phi \qquad \text{(A.16)}\\
b_{mn}&=\frac{2n+1}{2\pi}\frac{(n-m)!}{(n+m)!}\int_0^{2\pi}\int_0^{\pi}f(\theta,\phi)P_n^m(\cos\theta)\ \sin m\phi\ \sin\theta d\theta\, d\phi
\end{aligned}$$

To derive the orthogonality relationships of tesseral harmonics, we first assume two solutions to the scalar Helmholtz as

$$\begin{aligned}
\psi_1&=h_n^{(1)}(kr)\ T_{mn}^{i}(\theta,\phi)\\
\psi_2&=h_q^{(1)}(kr)\ T_{pq}^{j}(\theta,\phi)
\end{aligned} \quad \text{(A.17)}$$

where $T_{mn}^{i}(\theta,\phi)$ and $T_{pq}^{j}(\theta,\phi)$ are tesseral harmonics. For our proof we use Green's theorem, which is

$$\iint\left(\psi_1\frac{\partial\psi_2}{\partial n}-\psi_2\frac{\partial\psi_1}{\partial n}\right)ds=\iiint\left(\psi_1\nabla^2\psi_2-\psi_2\nabla^2\psi_1\right)d\tau \tag{A.18}$$

The right-hand side vanishes since ψ_1 and ψ_2 are well behaved solutions to the same Helmholtz equation. Next, applying (A.18) to a sphere of radius r, we have

$$r^2\int_0^{2\pi}\int_0^{\pi}\left(\psi_1\frac{\partial\psi_2}{\partial r}-\psi_2\frac{\partial\psi_1}{\partial r}\right)d\theta d\phi=0 \tag{A.19}$$

Substitute (A.17) into (A.19), we have

$$kr^2\left(h_n^{(1)}h_q'^{(1)}-h_n'^{(1)}h_q^{(1)}\right)\int_0^{2\pi}\int_0^{\pi}T_{mn}^iT_{pq}^j\sin\theta d\theta d\phi=0 \tag{A.20}$$

Furthermore, $kr^2\left(h_n^{(1)}h_q'^{(1)}-h_n'^{(1)}h_q^{(1)}\right)$ can be canceled out for arbitrary r only when $n=q$. Hence

$$\int_0^{2\pi}\int_0^{\pi}T_{mn}^i(\theta,\phi)T_{pq}^j(\theta,\phi)\sin\theta d\theta d\phi=0 \qquad \mathrm{n}\neq\mathrm{q} \tag{A.21}$$

Now we can separate the variable θ,ϕ in (A.21). For the ϕ integration, we have already known their orthogonality relationships

$$\begin{gathered}\int_0^{2\pi}\sin m\phi\cos p\phi\ d\phi=\int_0^{2\pi}\cos m\phi\sin p\phi\ d\phi=0\\ \int_0^{2\pi}\sin m\phi\sin p\phi\ d\phi=\int_0^{2\pi}\cos m\phi\cos p\phi\ d\phi=\begin{cases}0 & m\neq p\\ \pi & m=p\neq 0\end{cases}\end{gathered} \tag{A.22}$$

For the θ integration,

$$\begin{gathered}\int_0^{\pi}P_n(\cos\theta)P_q(\cos\theta)\ \sin\theta d\theta=0 \qquad n\neq q\\ \int_0^{\pi}\left[P_n(\cos\theta)\right]^2\ \sin\theta d\theta=\frac{2}{2n+1} \qquad n=q\end{gathered} \tag{A.23}$$

Finally, the overall orthogonality relationships of tesseral harmonics can be combined and expressed as

$$\int_0^{2\pi}\int_0^{\pi} T_{mn}^{e}(\theta,\phi)T_{pq}^{o}(\theta,\phi)\sin\theta d\theta\, d\phi = 0$$
$$\int_0^{2\pi}\int_0^{\pi} T_{mn}^{e}(\theta,\phi)T_{pq}^{e}(\theta,\phi)\sin\theta d\theta\, d\phi = 0 \tag{A.24}$$
$$\int_0^{2\pi}\int_0^{\pi} T_{mn}^{o}(\theta,\phi)T_{pq}^{o}(\theta,\phi)\sin\theta d\theta d\phi = 0 \qquad m,n \neq p,q$$

When m, $n = p$, q, we have

$$\int_0^{2\pi}\int_0^{\pi}\left[T_{mn}^{i}(\theta,\phi)\right]^2 \sin\theta d\theta\, d\phi = \begin{cases} \dfrac{4\pi}{2n+1} & m=0,\ i=e \\ \dfrac{2\pi}{2n+1}\dfrac{(n+m)!}{(n-m)!} & m \neq 0 \end{cases} \tag{A.25}$$

For any $f(\theta,\phi)$ on a sphere expressed as (A.15), we multiply each side by $T_{p,q}^{i}\sin\theta$, and integral over 0 to 2π on ϕ and 0 to π on θ. All terms except those have m, $n = p$, q vanish by (A.24), and by (A.23), the results state as (A.16) are proved.

Using (A.15) and (A.16), we can consequently derive the spherical wave coefficients B_{nm} as (2.11).

References

[1] P. Harrop, "Near field UHF vs. HF for item level tagging," IDTechEx article. Available:
http://www.eurotag.org/?Articles_and_Publications

[2] D. Desmons, "UHF Gen2 for item-level tagging," presentation at RFID World 2006. Available:
http://www.impinj.com/files/Impinj_ILT_RFID_WORLD.pdf

[3] C. Ajluni, "Item-level RFID takes off," RF Design magazine, Sep. 2006.

[4] S. Ortiz, Jr., "Is near-field communication close to success?" *IEEE Computer Society*, Vol. 39, pp. 18–20, Mar. 2006.

[5] J. Walko, "A ticket to ride," *IET Communications Engineer*, Vol. 3, pp. 11–14, Feb.-Mar. 2005.

[6] C. Evans-Pughe, "Close encounters of the magnetic kind," *The IEE Review*, Vol. 51, pp. 38–42, May 2005.

[7] S. Esko, K. Jouni, P. Juha, Y. Arto, and K. Ilkka, "Application of near field communication for health monitoring in daily life," *Engineering in Medicine and Biology Society, IEEE annual international conference*, pp. 3246–3249, Aug. 2006.

[8] S. Dominikus and M. Aigner, "mCoupons: An application for near field communication (NFC)," *Advanced Information Networking and Applications Workshops, 2007, AINAW'07. 21st International Conference*, vol. 2, pp. 421–428, May 2007.

[9] G. A. Wright, "Magnetic resonance imaging," *IEEE Signal Processing*, vol. 14, no. 1, pp. 118–125, Jan. 1997.

[10] K. Fotopoulou, B. W. Flynn, "Optimum antenna coil structure for inductive powering of passive RFID tags," *IEEE International Conference on RFID*, pp. 71–77, Mar. 2007.

[11] P. Cole, "Coupling relations in RFID systems," "Coupling relations in RFID systems II: Practical performance measurements," white papers, 2003. Available: http://www.autoidlabs.org/publications/page.html

[12] H. Schantz, "A near-field propagation law and a novel fundamental limit to antenna gain versus size," *IEEE Antenna & Propagation Society International Symposium*, vol. 3B, pp. 134–137, Jul. 2005.

[13] D. C. Yates, A. S. Holmes, and A. J. Burdett, “Optimal transmission frequency for ultralow-power short-range radio links,” *IEEE Trans. Circuits Syst. I*, vol. 51, no. 7, pp. 1405–1413, 2004.

[14] A. D. Yaghjian, “An overview of near-field antenna measurements,” *IEEE Trans. Antennas Propagat.*, vol. AP–34, pp. 30–45, Jan. 1986.

[15] A. D. Yaghjian, “Efficient computation of antenna coupling and fields within the near-field region,” *IEEE Trans. Antennas Propagat.*, vol. AP–30, pp. 113–128, Jan. 1982.

[16] R. F. Harrington, *Time-harmonic electromagnetic fields*, Wiley 2001, pp. 264–276.

[17] L. C. Andrews, *Special functions of mathematics for engineers, 2nd edition*, New York: McGraw-Hill, 1992, pp. 317–319.

[18] K. Finkenzeller, *RFID handbook: Radio–frequency identification fundamentals and applications, 2nd Edition*, Wiley, 2004.

[19] P. V. Nikitin, K. V. S. Rao, and S. Lazar, “An overview of near filed UHF RFID,” *IEEE International Conference on RFID*, pp. 167–174, Mar. 2007.

[20] K. Kurokawa, “Power waves and the scattering matrix,” *IEEE Trans. Microw. Theory Tech*, vol. MTT-13, no. 3, pp. 194–202, Mar. 1965.

[21] S. L. Chen, K. H. Lin, “A folded dipole with a close loop antenna for RFID applications,” *IEEE Antenna & Propagation Society International Symposium*, pp. 2281–2284, Jun. 2007.

[22] H. K. Ryu, J. M. Woo, “Size reduction in UHF band RFID tag antenna based on circular loop antenna,” Internal Conference on Applied Electromagnetics and Communications, Oct, 2005, pp. 1–4.

[23] Y. Qian, T. Itoh, “A broadband uniplanar microstrip-to-CPS transition,” *Microwave Conf. Proc. APMC’* 97, vol. 2,pp. 609–612, 1997.

[24] A. Rahmati, L. Zhong, “Reliability techniques for RFID-based object tracking Applications,” *IEEE Internal Conference on Dependable Systems and Networks (DSN’ 07)*, Jun. 2007, pp. 113–118.

[25] Industry Whitepaper, “RFID and UHF: A prescription for RFID success in the pharmaceutical industry,” 2006.
Available: http://www.pharmaceuticalonline.com/uhf/RFIDUHFAPrescriptionforRFIDSuccess.pdf

[26] S. R. Aroor and D. D. Deavous, “Evaluation of the state of passive UHF RFID: An experimental approach,” *IEEE Systems Journal*, vol. 1, pp. 168–176, Dec. 2007.